6 Photophysics of hexafluorobenzene

6.1 Introduction

Fluorine atom substitution in the Bz ring leads to a stabilization of the σ orbitals which consist mostly the fluorine orbitals. In a more general context this phenomenon is known as perfluoro effect in the literature [1]. Several experimental and theoretical studies on neutral FBz molecules have appeared in the literature over the past decades [2–24], a detailed understanding of the spectroscopic and dynamical properties of their electronic excited states is still missing. Despite this, some detailed theoretical studies attempting to understand these properties of neutral FBzs and their radical cations have appeared in the recent past [25–31]. In continuation to earlier works of this group on MFBz, *o*-DFBz, *m*-DFBz, PFBz [25,26] and $TFBz^+$ [30] we attempt here to investigate the structure and dynamics of the energetically low-lying electronic states of HFBz by quantum mechanical methods. Like the parent Bz, HFBz also belongs to the D_{6h} symmetry point group at its equilibrium geometry. Because of high symmetry like Bz, many optical transitions are electric-dipole forbidden in HFBz also. Vibronic interaction is an important mechanism that causes a symmetry mixing and allows optically dark transitions. This statement dates back to the work of Sponer *et al.* , in which the optically dark transition of Bz was reported [32] for the first time. Furthermore, because of high symmetry, many of the low-lying electronic states of these molecules are orbitally degenerate and prone to the JT distortion [33]. The latter introduces a rich variety of vibronic coupling mechanisms which are fundamentally important in the spectroscopic and dynamical properties of these polyatomic molecular systems.

Spectroscopic [9, 13] and photophysical [5, 7] studies on FBz molecules have revealed that the features of the electronic absorption and emission bands and lifetimes of fluorescence emission strongly depends on the number of substituted fluorine atoms. For example, C_6F_n with n $\leq$ 4 exhibit structured $S_1 \leftarrow S_0$ absorption band, large quantum yield and nanosecond lifetime of fluorescence. On the other hand, C_6F_n with n=5 and 6 exhibit structureless $S_1 \leftarrow S_0$ absorption band [9, 13], low quantum yield [5, 7], picosecond and nanosecond lifetime of fluorescence emission [16]. Furthermore, a biexponential decay of fluorescence is observed for the latter molecules [16]. Experimental measurements of Philis *et al.* [13] revealed that a lowering of D_{6h} symmetry of Bz by fluorine substitution leads to the appearance of additional bands within 8.0 eV which do not have a Bz parentage. For example, apart from three singlet-singlet transitions analogous to the $B_{2u} \leftarrow A_{1g}$, $B_{1u} \leftarrow A_{1g}$ and $E_{1u} \leftarrow A_{1g}$ transitions in Bz, one additional band has been observed in MFBz and in *o*-DFBz in the region of the $^1B_{1u}$ band [13]. This band is correlate with the 3s ($^1E_{1g}$) Rydberg state of Bz molecule [13]. Likewise,

one additional band has been identified in PFBz and HFBz at ∼5.85 and ∼5.36 eV, respectively, and is designated as the unassigned C-band [13]. Recent theoretical studies [25, 26] on the FBz molecules have settled the ambiguities over the justification of the origin of these additional bands and several other issues mentioned above for C_6F_n with n upto 5. It appears from the work done by Mondal *et al.* [25, 26] that along with vibronic coupling, perfluoro effect [1] also plays an important role on the dynamics of the low-lying excited electronic states of these FBz molecules. In case of HFBz (where all the hydrogen atoms are replaced by fluorine atoms and the perfluoro effect is expected to have the maximum impact), there exist no clear-cut understanding of the origin of the additional bands (when compared to Bz) and several anomalous experimental observations about it's fluorescence lifetime and biexponential decay dynamics in gas phase absorption spectrum [13]. Furthermore, the additional band (C-band) observed in HFBz, unlike PFBz, exhibits a twin structure and there is no unambiguous interpretation exists for the observed twin to date.

The lowering of energy of the two lowest $\pi\sigma^*$ states upon increasing fluorination is discussed in our previous work [25]. For completeness, we plot in Fig. 6.1, the energy of the first few electronic states of Bz and HFBz calculated at the equilibrium geometry of the respective S_0 state. The energies are calculated by the EOM-CCSD method using the aug-cc-pVDZ basis set. It can be seen from the diagram that the $\pi\sigma^*$ state becomes S_2 in case of HFBz. In the latter, two $\pi\sigma^*$ states are degenerate at the equilibrium configuration of the S_0 state. They represent the two components of the degenerate $^1E_{1g}$ electronic state of HFBz [25]. These findings are in excellent accord with those of Philis *et al.* [13], Motch *et al.* [20] and Holland *et al.* [21] but are in contrast to those of Zgierski *et al.* [19] and Temps *et al.* [22]. The lowest $\pi\sigma^*$ state was found to be the S_1 (in PFBz and HFBz) in the latter studies [19, 22].

The absorption bands observed within 8.0 eV for HFBz are highly diffuse and exhibit irregular structures which hardly allow any definitive vibrational assignments. Therefore, a detail theoretical investigation of the nuclear dynamics is undertaken to understand the these observations. The complex and diffuse nature of the gas phase absorption spectrum of HFBz [13, 19–22] suggests vibronic coupling among the underlying excited electronic states which makes an optically dark transition allowed. Such coupling induces nonadiabatic transitions among different electronic states and a mixing of the energy levels of different vibronic symmetries. A typical signature of vibronic interactions is the occurrence of CIs [34, 37–42] of electronic PESs in multi-dimensions. These intersections become the mechanistic bottleneck for ultrafast relaxation and energy transfer between electronic states [34]. Occurrence of CIs causes a breakdown of the adiabatic BO approximation [43]. The nonadiabatic coupling terms are singular in the adiabatic electronic basis. For numerical convenience, a diabatic electronic basis [44] is preferred in the dynamics study. In the latter basis, the coupling between states is described by the electronic Hamiltonian and the coupling elements are smooth functions of nuclear coordinates.

The aim of the present chapter is to understand some of the unresolved issues on the observed optical absorption spectrum of HFBz and to provide a comparative account on the impact of fluorine atom substitution on the optical absorption spectrum

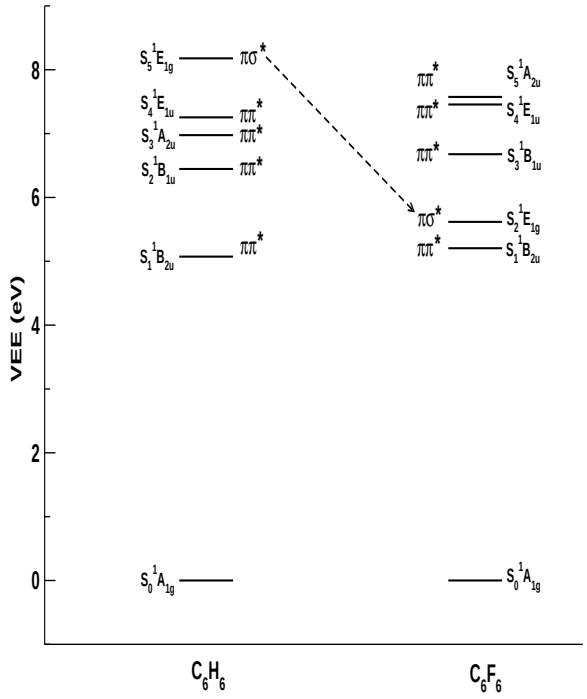

Figure 6.1: Schematic diagram of the energetically low-lying electronic states of Bz and HFBz. The adiabatic electronic energies are calculated at the equilibrium configuration of the respective S_0 state. The zero of energy corresponds to the equilibrium minimum of the S_0 state of Bz and HFBz. Further details of the diagram are given in Sec. 6.2 of the text.

of Bz. This task is accomplished by performing detail *ab initio* electronic structure calculations and first principles simulations of nuclear dynamics. The electronic structure calculations for the low-lying electronic states of HFBz are carried out to construct an appropriate parametrized model vibronic Hamiltonian of HFBz. In this model the PESs and the coupling surfaces of the relevant electronic states are constructed by calculating the VEEs with the aid of EOM-CCSD method [45] implemented in MOLPRO suite of program [46]. The VEEs are calculated along the dimensionless normal displacement coordinates of all the vibrational modes. The calculated adiabatic energy points are fitted to the theoretical model developed in this chapter. The coupling between different electronic states is taken into consideration in accordance with the symmetry selection rules [54] and the relative phases of the coupling terms of the Hamiltonian are derived from group theory considerations analogous to that carried out for the benzene radical cation (Bz^+) [35].

On the technical aspects, a time-independent matrix diagonalization approach to treat the coupled-state nuclear dynamics including all the relevant vibrational modes is beyond the capability of the present computer hardware. This task is therefore accomplished with a time-dependent WP propagation approach employing the MCTDH scheme developed at Heidelberg [47–50]. This scheme has been very successful particularly in treating

the multi-state and multi-mode vibronic coupling problems of large dimension [47–50]. While the final results of this chapter are obtained by this method, comparison calculations are carried out in reduced dimensions by the time-independent matrix diagonalization method in order to arrive at unambiguous assignments (whenever possible) of the vibronic structure of the observed absorption bands.

6.2 Details of electronic structure calculations

The reference equilibrium geometry of the electronic ground state [S_0 ($^1A_{1g}$)] of HFBz is optimized by the MP2 theory method employing the aug-cc-pVDZ basis set of Dunning [51]. The Gaussian-03 suite of program [52] is used for this purpose. The optimized reference equilibrium geometry converged to the D_{6h} symmetry point group. The optimized structural parameters, $r_{C-C} = 1.401$ angstrom and $r_{C-F} = 1.346$ angstrom, are in fair agreement with their experimental values [53] of, 1.391 ± 0.007 angstrom and 1.327 ± 0.007 angstrom, respectively.

Harmonic frequency (ω_i) of the vibrational modes of HFBz is calculated by diagonalizing the kinematic and *ab initio* force constant matrix of the reference equilibrium structure. These vibrational frequencies are listed in Table 6.1. The mass-weighted normal coordinates of the vibrational modes are calculated from the eigenvectors of the force constant matrix. These are then transformed into their dimensionless form ($\mathbf{Q}_i$) by multiplying with $\sqrt{\omega}_i$ (in a_0). The fundamental vibrational modes of HFBz belong to ten degenerate and ten nondegenerate symmetry species of the D_{6h} point group. They decompose into the following IREPs of this symmetry point group [54]:

$$\begin{aligned}\Gamma &= 2a_{1g}(\nu_1,\nu_2) \oplus a_{2g}(\nu_3) \oplus a_{2u}(\nu_4) \oplus 2b_{1u}(\nu_5,\nu_6) \oplus 2b_{2g}(\nu_7,\nu_8) \oplus 2b_{2u}(\nu_9,\nu_{10}) \oplus \\ &\quad e_{1g}(\nu_{11}) \oplus 3e_{1u}(\nu_{12},\nu_{13},\nu_{14}) \oplus 4e_{2g}(\nu_{15},\nu_{16},\nu_{17},\nu_{18}) \oplus 2e_{2u}(\nu_{19},\nu_{20}). \qquad (6.1)\end{aligned}$$

The description of the vibrational modes of Eq. (6.1) is given in Table 6.1 along with their numbering as proposed by Herzberg [55] and also by Wilson [56].

Adiabatic energies of the low-lying singlet electronic states of HFBz are calculated *ab initio* along the dimensionless normal coordinates of the 30 (altogether) vibrational degrees of freedom. The VEEs of these electronic states are calculated for $Q_i = \pm 0.25$ and in the range -3.00 to $+3.00$ with an increment 0.50, along i^{th} vibrational mode (keeping others at their equilibrium value) using the EOM-CCSD method as implemented in MOLPRO program package [46]. Like in our previous studies on FBzs [25,26,30] the aug-cc-pVDZ basis set is used for the C atoms and the energy-consistent pseudopotentials of Stuttgart/Cologne group [58] are used for the fluorine atoms.

In order to ensure a reliable basis for using ECPs for fluorine atoms, we have done test calculations of the VEEs of the low-lying electronic states of HFBz with and without ECPs. The results are given in Table 6.2. It can be seen that the change in VEE for all five states is very minor (the average deviation is $\sim$0.04 eV), indicating the reliability of ECPs to describe the excited state PESs of HFBz.

Table 6.1: Description of the vibrational modes of the electronic ground state of HFBz calculated at the MP2/aug-cc-pVDZ level of theory.

Symmetry	Nomenclature		Vibrational Frequency(ω_i/eV)		Predominant nature
	Herzberg [55]	Wilson [56]	present	Experiment [57]	
a_{1g}	ν_1	ν_1	0.1874	0.1847	C-F stretching in-phase
	ν_2	ν_2	0.0686	0.0693	Ring breathing
a_{2g}	ν_3	ν_3	0.0968	0.0857	C-F in-plane bending, in-phase
a_{2u}	ν_4	ν_{11}	0.0261	0.0267	C-F out-of-plane bending, in-phase
b_{1u}	ν_5	ν_{12}	0.1507	0.1640	C-F trigonal stretching
	ν_6	ν_{13}	0.0727	0.0793	C-C-C trigonal bending
b_{2g}	ν_7	ν_4	0.0577	0.0885	C-F out-of-plane trigonal
	ν_8	ν_5	0.0222	0.0309	C-C-C Puckering
b_{2u}	ν_9	ν_{14}	0.1825	0.1553	C-C stretching (kekule)
	ν_{10}	ν_{15}	0.0341	0.0258	C-F in plane trigonal bending
e_{1g}	ν_{11}	ν_{10}	0.0448	0.0459	C-F out-of-plane bending
e_{1u}	ν_{12}	ν_{20}	0.1921	0.1897	C-C stretching
	ν_{13}	ν_{19}	0.1236	0.1263-0.1232	C-F stretching
	ν_{14}	ν_{18}	0.0387	0.0391	C-F in-plane bending
e_{2g}	ν_{15}	ν_6	0.2093	0.2052	C-C stretching
	ν_{16}	ν_9	0.1420	0.1434	C-F stretching
	ν_{17}	ν_8	0.0541	0.0549	C-C-C in-plane bending
	ν_{18}	ν_7	0.0328	0.0327	C-F in-plane bending
e_{2u}	ν_{19}	ν_{16}	0.0757	0.0738	C-C-C out-of-plane
	ν_{20}	ν_{17}	0.0169	0.0217	C-F out-of-plane

Table 6.2: Vertical excitation energy (in eV) of the five low-lying four excited singlet electronic states calculated at the equilibrium geometry of S_0 state of HFBz.

State	aug-cc-pVDZ	ECP
$S_1(^1B_{2u})$	5.204	5.168
$S_2(^1E_{1g})$	5.617	5.678
$S_3(^1B_{1u})$	6.677	6.646
$S_4(^1A_{2u})$	7.456	7.556
$S_5(^1E_{1u})$	7.574	7.542

6.3 The vibronic Hamiltonian and nuclear dynamics

In this section we construct a Hamiltonian in the normal displacement coordinates of the reference electronic ground state of HFBz in accordance with the symmetry selection rule. The nuclear dynamics in its excited electronic states is studied subsequently using this Hamiltonian. The Hamiltonian is constructed in a diabatic electronic basis [44]. Within $\sim$ 8.0 eV excitation energy range signature of five excited singlet electronic states (viz., $S_1{}^1B_{2u}$, $S_2{}^1E_{1g}$, $S_3{}^1B_{1u}$, $S_4{}^1E_{1u}$ and $S_5{}^1A_{2u}$) emerged in the experimental absorption spectrum [13]. The symmetry of these electronic states indicates that the JT and PJT interactions are the two fundamentally important mechanisms that would primarily govern the overall shape and the assignment of the electronic absorption bands of HFBz. With the given symmetry representation of the electronic states and the vibrational modes, the following rules can be derived from the character table of the D_{6h} symmetry point group.

The first-order coupling within (intra) and between (inter) electronic states is governed by the selection rules; $(\Gamma_i)^2 \supset (\Gamma_{a_1})$ and $\Gamma_i \otimes \Gamma_j \supset \Gamma_x$, respectively [34]. The symbol, Γ represents the IREP, i and j are the electronic state indices, a_1 represents the totally symmetric vibrational mode and the symbol, x, represents the symmetry of the vibrational mode that transforms according to, $\Gamma_i \otimes \Gamma_x \otimes \Gamma_j \supset A_1$. Now for the degener-

ate, $^1E_{1g}$ (S_2) and $^1E_{1u}$ (S_4) electronic states the symmetrized direct product transforms into, $(E_{1g})^2 = (E_{1u})^2 = a_{1g} + e_{2g}$. While the vibrational modes of a_{1g} symmetry can not split the electronic degeneracy (are condon active), the modes of e_{2g} symmetry can lift this electronic degeneracy and are JT active. For the rest of the off-diagonal elements of the Hamiltonian written below the following symmetry rules apply.

$$B_{2u} \otimes E_{1g} = e_{2u}\ (\nu_{19}, \nu_{20}), \tag{6.2a}$$
$$B_{2u} \otimes B_{1u} = a_{2g}\ (\nu_3), \tag{6.2b}$$
$$B_{2u} \otimes E_{1u} = e_{2g}\ (\nu_{15}, \nu_{16}, \nu_{17}, \nu_{18}), \tag{6.2c}$$
$$B_{2u} \otimes A_{2u} = b_{1g}, \tag{6.2d}$$
$$E_{1g} \otimes B_{1u} = e_{2u}\ (\nu_{19}, \nu_{20}), \tag{6.2e}$$
$$E_{1g} \otimes E_{1u} = e_{2u}\ (\nu_{19}, \nu_{20}) + a_{2u}\ (\nu_4) + a_{1u}, \tag{6.2f}$$
$$E_{1g} \otimes A_{2u} = e_{1u}\ (\nu_{12}, \nu_{13}, \nu_{14}), \tag{6.2g}$$
$$B_{1u} \otimes E_{1u} = e_{2g}\ (\nu_{15}, \nu_{16}, \nu_{17}, \nu_{18}), \tag{6.2h}$$
$$B_{1u} \otimes A_{2u} = b_{2g}\ (\nu_7, \nu_8), \tag{6.2i}$$
$$E_{1u} \otimes A_{2u} = e_{1g}\ (\nu_{11}). \tag{6.2j}$$

According to Eq. (6.1) HFBz does not have any vibrational mode of either b_{1g} or a_{1u} symmetry. Therefore, the coupling of the electronic states as given in Eqs. (6.2d) and (6.2f), through these modes do not appear in the electronic Hamiltonian given below. The relative sign of various elements of the Hamiltonian is determined by explicitly checking the invariance of the Hamiltonian with respect to the symmetry operations of the D_{6h} point group, following similar works on Bz and cyclopropane radical cation [35, 36]. With these considerations the vibronic Hamiltonian can be written as

$$\mathcal{H} = \mathcal{H}_0 \mathbf{1}_7 + \mathcal{W}, \tag{6.3a}$$

where

$$\mathcal{W} = \begin{bmatrix}
\mathcal{E}^1 + \mathcal{U}^1 & \sum_{i\in e_{2u}} \lambda_i^{1,2x} Q_{ix} & \sum_{i\in e_{2u}} -\lambda_i^{1,2y} Q_{iy} & \sum_{i\in a_{2g}} \lambda_i^{1,3} Q_i & \sum_{i\in e_{2g}} \lambda_i^{1,4x} Q_{ix} & 0 & \sum_{i\in e_{2g}} -\lambda_i^{1,4y} Q_{iy} \\
h.c. & \mathcal{E}^2 + \mathcal{U}^{2x} & \sum_{i\in e_{2g}} \lambda_i^{2x,2y} Q_{iy} & \sum_{i\in e_{2u}} \lambda_i^{2x,3} Q_{ix} & \sum_{i\in a_{2u}} \lambda_i^{2x,4x} Q_i & \sum_{i\in e_{1u}} \lambda_i^{2x,5} Q_{ix} & \sum_{i\in e_{2u}} \lambda_i^{2x,4y} Q_{iy} + \sum_{i\in a_{1u}} \lambda_i^{2x,4y} Q_i \\
 & h.c. & \mathcal{E}^2 + \mathcal{U}^{2y} & \sum_{i\in e_{2u}} -\lambda_i^{2y,3} Q_{iy} & \sum_{i\in e_{2u}} \lambda_i^{2y,4x} Q_{iy} - \sum_{i\in e_{1u}} \lambda_i^{2y,4x} Q_i & \sum_{i\in e_{1u}} -\lambda_i^{2y,5} Q_{iy} & \sum_{i\in e_{2u}} \lambda_i^{2y,4y} Q_{ix} + \sum_{i\in a_{2u}} \lambda_i^{2y,4y} Q_i \\
 & & h.c. & \mathcal{E}^3 + \mathcal{U}^3 & \sum_{i\in e_{2g}} \lambda_s^{3,4x} Q_{ix} & \sum_{i\in b_{2g}} \lambda_i^{3,5} Q_i & \sum_{i\in e_{2g}} -\lambda_i^{3,4y} Q_{iy} \\
 & & & h.c. & \mathcal{E}^{4x} + \mathcal{U}^{4x} & \sum_{i\in e_{1g}} \lambda_i^{4x,5} Q_{ix} & \sum_{i\in e_{2g}} \lambda_i^{4x,4y} Q_{iy} \\
 & & & & h.c. & \mathcal{E}^5 + \mathcal{U}^5 & \sum_{i\in e_{1g}} -\lambda_i^{4y,5} Q_{iy} \\
 & & & & & h.c. & \mathcal{E}^{4y} + \mathcal{U}^{4y}
\end{bmatrix} \tag{6.3b}$$

In the above, $\mathcal{H}_0 = \mathcal{T}_N + \mathcal{V}_0$, represents the Hamiltonian (assumed to be harmonic) of the reference electronic ground (S_0) state of HFBz with

$$\mathcal{T}_N = -\frac{1}{2}\sum_{i\ \in\ a_{1g},\ a_{2g},\ b_{2g},\ b_{2u}} \omega_i \frac{\partial^2}{\partial Q_i^2} - \frac{1}{2}\sum_{i\ \in\ e_{2g},\ e_{2u},\ e_{1g},\ e_{1u}} \omega_i \left(\frac{\partial^2}{\partial Q_{ix}^2} + \frac{\partial^2}{\partial Q_{iy}^2}\right), \quad (6.4)$$

and

$$\mathcal{V}_0 = \frac{1}{2}\sum_{i\ \in\ a_{1g},\ a_{2g},\ b_{2g},\ b_{2u}} \omega_i Q_i^2 + \frac{1}{2}\sum_{i\ \in\ e_{2g},\ e_{2u},\ e_{1g},\ e_{1u}} \omega_i \left(Q_{ix}^2 + Q_{iy}^2\right). \quad (6.5)$$

The quantity $\mathbf{1_7}$ is a 7×7 diagonal unit matrix. The nondiagonal matrix Hamiltonian in Eq. (6.3b) describes the PESs of the excited electronic states of HFBz and their coupling surfaces. The quantity $\mathcal{E}^j$ in this matrix is the VEE of the j^{th} electronic state. The elements of this matrix are expanded in a standard Taylor series around the reference equilibrium geometry at, $\mathbf{Q} = \mathbf{0}$, in the following way

$$\mathcal{U}^j = \sum_{i\ \in\ a_{1g}} \kappa_i^j Q_i + \frac{1}{2}\sum_{i\ \in\ a_{1g},\ a_{2g},\ b_{2g},\ b_{2u}} \gamma_i^j Q_i^2 + \frac{1}{2}\sum_{i\ \in\ e_{2g},\ e_{2u},\ e_{1g},\ e_{1u}} [\gamma_i^j (Q_{ix}^2 + Q_{iy}^2)] + \frac{1}{24}[\zeta_{15}^{(3)}(Q_{15x}^4 + Q_{15y}^4)]; j \in 1, 3 \text{ and } 5, \quad (6.6a)$$

$$\mathcal{U}^{jx/jy} = \sum_{i\ \in\ a_{1g}} \kappa_i^j Q_i \pm \sum_{i\ \in\ e_{2g}} \lambda_i^j Q_{ix} + \frac{1}{2}\sum_{i\ \in\ a_{1g},\ a_{2g},\ b_{2g},\ b_{2u}} \gamma_i^j Q_i^2 + \frac{1}{2}\sum_{i\ \in\ e_{2g},\ e_{2u},\ e_{1g},\ e_{1u}} [\gamma_i^j (Q_{ix}^2 + Q_{iy}^2)]; j \in 2 \text{ and } 4. \quad (6.6b)$$

In above equations the two components of the degenerate states and modes are labeled with x/y. The quantity κ_i^j and λ_i^j represents the linear intrastate and interstate (JT) coupling parameters [34] for the symmetric (a_{1g}) and degenerate (e_{2g}) vibrational modes, respectively, for the j^{th} electronic state. The first-order PJT coupling parameter of the i^{th} vibrational mode between the electronic states j and k is given by λ_i^{j-k}; γ_i^j and ζ_i^j are the second-order and fourth-order coupling parameters of the i^{th} vibrational mode for the j^{th} electronic state. The summations run over the normal modes of vibration of specified symmetry in the index. The + and - sign in Eq. (6.6b) is applicable to the x and y components of the degenerate state, respectively. A fourth-order term along the degenerate ν_{15} vibrational mode is included in Eq. (6.6a), in order to account for the anharmonicity of the S_3 state along this vibrational mode (discussed later in the text). The VEEs calculated in Sec. 6.2 are fitted to the adiabatic counterpart of diabatic electronic Hamiltonian of Eq. 6.3 by a least squares procedure to estimate the parameters of the Hamiltonian defined above. The estimated parameters along the relevant vibrational modes are given in Tables 6.3 and 6.4. A careful inspection of the

coupling parameters suggests that not all 30 vibrational modes play significant role in the nuclear dynamics on the electronic states of HFBz considered in this chapter. Therefore, only the relevant modes having significant coupling strengths are retained in the nuclear dynamics study presented below. The VEEs of the electronic excited states of HFBz are given in Table 6.5 along with the theoretical and experimental excitation energies available from the literature.

Table 6.3: Ab initio calculated linear and quadratic coupling constants for the $S_1{}^1B_{2u}$, $S_2{}^1E_{1g}$, $S_3{}^1B_{1u}$, $S_4{}^1E_{1u}$ and $S_5{}^1A_{2u}$ electronic states of HFBz. All data are given in the eV unit.

Symm-etry	Mode	κ_i	γ_i	κ_i or λ_i	γ_i	κ_i	γ_i	κ_i or λ_i	γ_i	κ_i	γ_i
		S_1		S_2		S_3		S_4		S_5	
a_{1g}	ν_1	-0.1565 (0.3)	0.0059	0.0791(0.1)	-0.0288	-0.1357(0.3)	0.0038	-0.1467(0.3)	0.0001	-0.0225(0.0)	-0.0587
	ν_2	-0.1055 (1.2)	-0.0022	-0.0517(0.3)	-0.0038	-0.0827(0.7)	0.0008	-0.0931(0.9)	-0.0023	-0.0576(0.4)	-0.0085
a_{2g}	ν_3		-0.0068		-0.0113		-0.0062		-0.0075		-0.0143
a_{2u}	ν_4		-0.0125		-0.0143		-0.0114		-0.0169		-0.0063
b_{1u}	ν_5		-0.0007		-0.0374		-0.0017		-0.0042		-0.0212
	ν_6		-0.0011		-0.0222		-0.0045		-0.0056		-0.0174
b_{2g}	ν_7		-0.0510		-0.0266		-0.0494		-0.0530		0.0212
	ν_8		-0.0144		-0.0193		-0.0174		-0.0145		0.00001
b_{2u}	ν_9		0.1514		0.0501		0.0691		0.0624		0.0139
	ν_{10}		0.0009		-0.0006		0.0004		-0.0007		-0.0058
e_{1g}	ν_{11}		-0.0643		0.0301		-0.0749		-0.1505		-0.2649
e_{1u}	ν_{12}		-0.0080		-0.0610		-0.0131		-0.0260		-0.0359
	ν_{13}		-0.0038		-0.0199		-0.0045		-0.0136		-0.0218
	ν_{14}		-0.0008		-0.0096		-0.0013		-0.0024		-0.0037
e_{2g}	ν_{15}		0.0147	0.1490(0.26)	-0.0167		0.0758	0.0672(0.06)	0.0476		-0.0310
	ν_{16}		-0.0007	0.0380(0.04)	-0.0285		-0.0233	0.0112(0.01)	0.0091		-0.0274
	ν_{17}		-0.0130	0.0717(0.88)	-0.0119		-0.0112	0.0195(0.06)	-0.0018		-0.0115
	ν_{18}		-0.0032	0.0309(0.44)	-0.0027		-0.0036	0.0075(0.02)	-0.0010		-0.0081
e_{2u}	ν_{19}		-0.0622		-0.0575		-0.0071		-0.0527		-0.0338
	ν_{20}		-0.0151		-0.0090		0.0060		-0.0141		-0.0134

Table 6.4: The interstate coupling parameters (in eV) of the vibronic Hamiltonian of Eq. 6.3 for the $S_1{}^1B_{2u}$, $S_2{}^1E_{1g}$, $S_3{}^1B_{1u}$, $S_4{}^1E_{1u}$ and $S_5{}^1A_{2u}$ electronic states of HFBz, estimated from the *ab initio* electronic structure results (see text for details).

Mode	$\lambda_i^{1,2}$	$\lambda_i^{1,3}$	$\lambda_i^{1,4}$	$\lambda_i^{2,3}$	$\lambda_i^{2,5}$	$\lambda_i^{3,4}$	$\lambda_i^{3,5}$	$\lambda_i^{4,5}$
ν_3		0.0139 (0.01)						
ν_7							0.1649 (3.92)	
ν_8							0.0526 (4.01)	
ν_{11}								0.1022 (2.60)
ν_{12}					0.1110 (0.09)			
ν_{13}					-			
ν_{14}					0.0631 (0.94)			
ν_{15}			0.2003 (0.44)			0.2610 (0.78)		
ν_{16}			0.0820 (0.16)			0.0902 (0.20)		
ν_{17}			0.0814 (1.14)			0.0470 (0.38)		
ν_{18}			0.0326 (0.50)			0.0244 (0.28)		
ν_{19}	0.1548 (2.10)							
ν_{20}	0.0619 (6.70)			0.0626 (6.86)				

Table 6.5: Vertical excitation energies (in eV) of the lowest five electronic states of HFBz.

	S_1 ($^1B_{2u} \leftarrow \tilde{X}\ ^1A_{1g}$) $\pi^* \leftarrow \pi$	S_2 ($^1E_{1g} \leftarrow \tilde{X}\ ^1A_{1g}$) $\sigma^* \leftarrow \pi$	S_3 ($^1B_{1u} \leftarrow \tilde{X}\ ^1A_{1g}$) $\pi^* \leftarrow \pi$	S_4 ($^1E_{1u} \leftarrow \tilde{X}\ ^1A_{1g}$) $\pi^* \leftarrow \pi$	S_5 ($^1A_{2u} \leftarrow \tilde{X}\ ^1A_{1g}$) $\pi^* \leftarrow \pi$
Ref. [11]	4.80	5.32	6.36	7.10	-
Ref. [14]	4.70	5.39	6.25	7.00	-
	-	5.72	-	-	-
Ref. [13, 15]	(4.28)	5.38	6.40	7.11	7.70
	-	5.75	-	-	-
Ref. [20]	4.86	5.38	6.39	7.11	7.70
	-	5.66	-	-	-
Ref. [21] EXPT	4.86	5.38	6.37	7.095	7.70
Ref. [21] TDDFT	4.91	5.05	5.90	-	-
Ref. [19] EXPT	4.48	4.34	4.90		
Ref. [19] TD/BP86	4.915	4.539	-	-	-
Ref. [22] TD/BP86	5.025	4.641	5.853	-	-
This work	5.168	5.678	6.646	7.542	7.556
Adjusted VEEs	5.032	5.594	6.776	7.256	7.706

6.4 Potential energy surfaces

In this section we examine the topography of the adiabatic PESs of the ground and first five excited singlet electronic states of HFBz obtained by diagonalizing the electronic Hamiltonian of the diabatic model developed above. The complex features of the vibronic bands recorded in the experiment [12, 13, 19–22] and the relaxation mechanisms are governed by the detail topography of these electronic states. One dimensional cuts of the full dimensional potential energy hypersurfaces of HFBz viewed along the given vibrational mode keeping others at their equilibrium values at, $\mathbf{Q}$=0, are shown in Figures 6.2 and 6.3. In these figures the solid curves represent the adiabatic potential energy functions obtained from the model developed in Sec 6.3 and the points superimposed on them are obtained from *ab initio* quantum chemical calculations discussed in Sec. 6.2.

In Figs. 6.2(a-b), the potential energies of the S_0, S_1, S_2, S_3, S_4 and S_5 electronic states (indicated in the panel) are plotted along the symmetric vibrational modes ν_1 and ν_2, respectively. It can be seen that the model reproduces the calculated *ab initio* data extremely well. The degeneracy of the S_2 and S_4 state remains unperturbed upon distortion along these symmetric vibrational modes. While the crossing of S_0 state with S_1 seems not very important, the crossing of S_1 and S_2 electronic states (panel a) appears to be important for the detailed structure of the first vibronic band. We note that these states are largely separated in the parent Bz molecule and therefore a structured S_1 band observed for this molecule [13] (cf. Fig. 6.1 drawn at the vertical configuration). The curve crossing between the S_1 and S_2 electronic states seen in Fig. 6.2(a) along ν_1 leads to energetically low-lying accessible CIs in multi-dimensions. It is to be noted again that, the S_1 state is of $\pi\pi^*$ origin where as, the S_2 state is of $\pi\sigma^*$ type. The schematic diagram given in Fig. 6.1 reveals that the $\pi\sigma^*$ state comes down in energy drastically (compared to the parent Bz molecule) due to perfluoro effect. Now it is intriguing to note that [cf. Fig. 6.2(a)] S_1 and S_2 state indeed cross at a distorted (from the reference equilibrium) geometry of HFBz. A similar situation was encountered in case of PFBz molecule, although the curve crossing was found at a much larger displacement from the vertical configuration for this molecule [25, 26]. The S_1 and S_2 states of HFBz are coupled (in first-order) through the PJT type of interactions by the vibrational modes ν_{19} and ν_{20} of e_{2u} symmetry (cf. Table 6.4). The two $\pi\sigma^*$ states become energetically

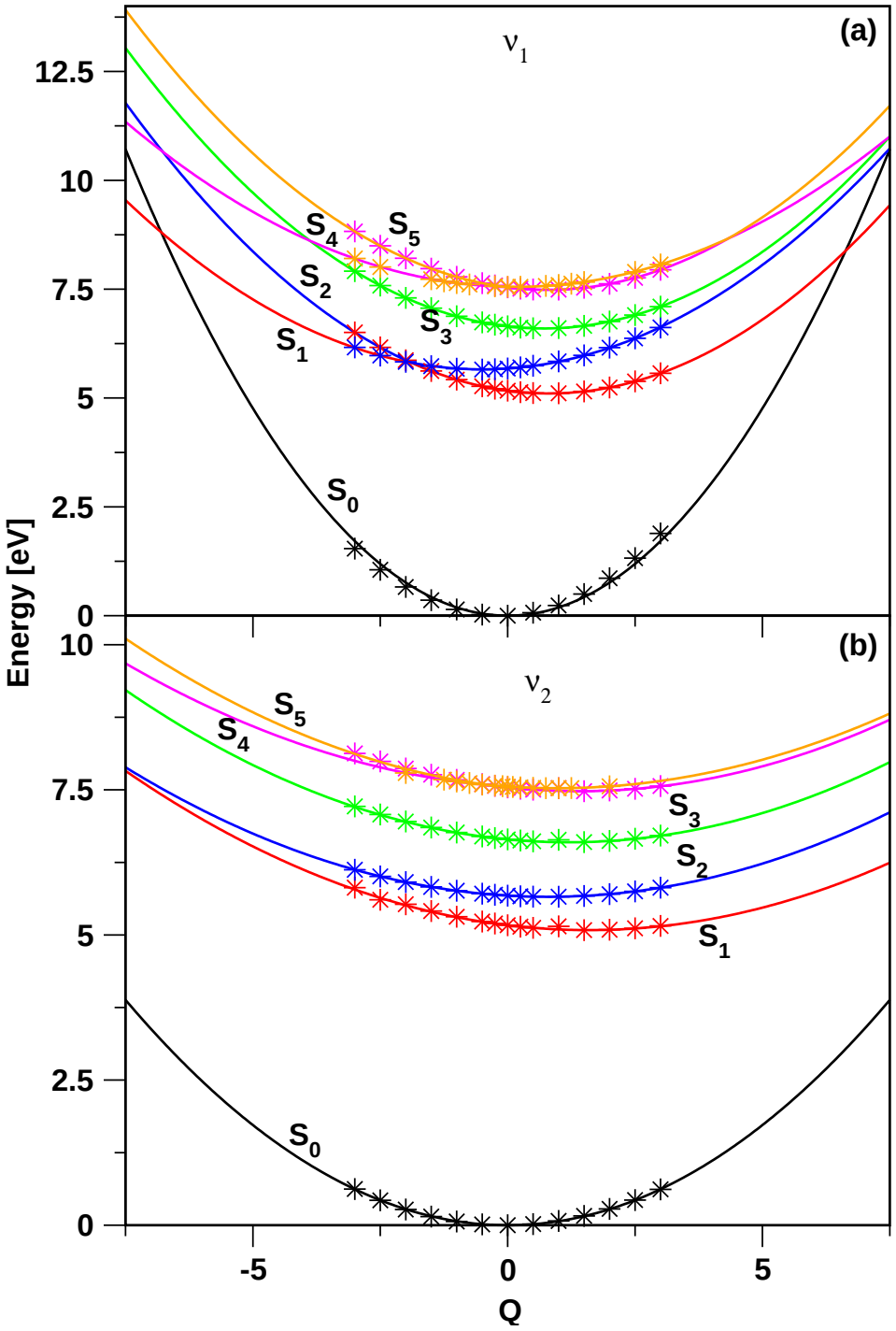

Figure 6.2: Adiabatic potential energies of ground and low-lying excited singlet electronic states of HFBz, along the normal coordinates of totally symmetric vibrational modes. The potential energies obtained from the present vibronic model are shown by the solid lines and the computed *ab initio* energies are shown by the asterisks.

degenerate and form the JT active S_2 state of HFBz. Apart from S_2, S_4 is also a JT ative state in HFBz. This state undergoes PJT crossings with the S_3 and S_5 states as clearly revealed by the potential energy curves shown in Fig. 6.2(a). In contrast to ν_1, the curve crossings are seldom visible along ν_2 in Fig. 6.2(b). The near degeneracy of the S_4 and S_5 states around the reference equilibrium configuration can be clearly seen from both the panels (a and b) of Fig. 6.2.

The locus of the degeneracy of the two components of the S_2 and also S_4 electronic states defines the seam of the JT CIs within these degenerate electronic states at the D_{6h} symmetry configuration of HFBz. Including the second-order diagonal coupling terms of symmetric modes, the energetic minimum on these seams is found at ∼5.64 and ∼7.42 eV for the S_2 and S_4 electronic state, respectively. The electronic degeneracy of the S_2 and S_4 state is split upon distortion along the degenerate (e_{2g}) vibrational modes $\nu_{15} - \nu_{18}$. This leads to a total of seven states altogether to be considered to treat the nuclear dynamics in the S_1-S_2-S_3-S_4-S_5 coupled electronic manifold of HFBz. The potential energies of these electronic states of HFBz are shown in Figs. 6.3(a-d) along the x component of the degenerate vibrational modes $\nu_{15} - \nu_{18}$, respectively. The symmetry rule forbids a first-order coupling of these vibrational modes in the nondegenerate S_1, S_3 and S_5 electronic states. However, these modes are JT active in first-order in the S_2 and S_4 electronic states. It can be seen from Fig. 6.3 that, the JT splitting is very small in the S_4 electronic state in contrast to a relatively larger splitting found in the S_2 state. Moreover, the quartic term of the Taylor expansion (Eqs. 6.6a) seems to have significant role in representing the potential energies of the S_3 state, along the vibrational mode of ν_{15}. It is well known that the JT distortion causes a symmetry breaking [34,40] and as a result the new minima on the lower adiabatic sheet of the JT split S_2 and S_4 states occur at ∼5.50 and ∼7.41 eV, respectively. The JT stabilization energies amount to ∼0.14 and ∼0.01 eV, respectively, for these two degenerate electronic states in that order.

It is obvious from the potential energy plots given in Figs. 6.3(a) and 6.3(b) (above) that, apart from the JT interactions within the degenerate electronic states (S_2 and S_4), curve crossings of the nondegenerate electronic states (S_1, S_3 and S_5) either among themselves or with the components of the JT split degenerate electronic states also exist. The latter describes the PJT interactions and the energetic minimum of the seam of S_1-S_2 PJT CIs is found at ∼ 5.51 eV. This minimum is ∼ 0.13 eV below the seam of JT CIs within the S_2 electronic manifold. The minimum of the S_2-S_3 CIs is found at ∼ 1.65 eV above the minimum of the JT CIs within the S_2 electronic manifold. This minimum is ∼ 0.60 eV above the minimum of the S_3 electronic state. Likewise, the minimum of the S_3-S_5 and S_4-S_5 CIs occurs at ∼ 1.08 and ∼ 0.01 eV above the minimum of the S_5 electronic state. We reiterate that the potential energy curves of Fig. 6.3 also confirms the near degeneracy of the S_4 and S_5 electronic states around the reference equilibrium configuration of HFBz. The energetic proximity of the minimum of an intersection seam to the equilibrium minimum of a state plays very important role in the nuclear dynamics as discussed below.

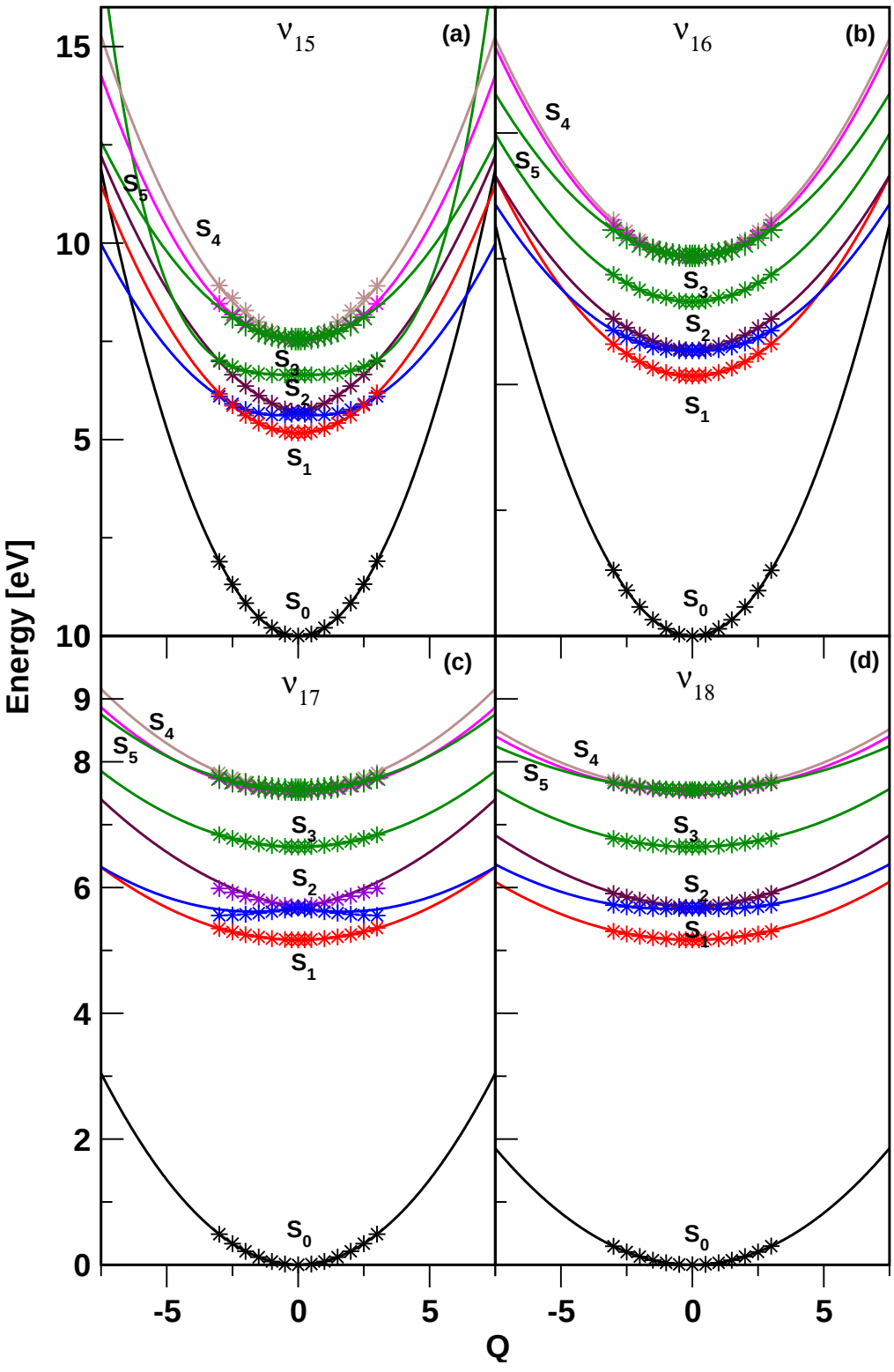

Figure 6.3: Same as in Fig. 6.2, along the dimensionless normal coordinates of the x component of the degenerate e_{2g} vibrational modes ν_{15}-ν_{18}.

6.5 Electronic absorption spectrum

As stated in the introduction, spectroscopic [9, 13] and photophysical [5, 7] studies have revealed that C_6F_n with n $\leq$ 4 exhibits structured $S_1 \leftarrow S_0$ absorption band where as,C_6F_n with n=5 and 6 exhibits structureless $S_1 \leftarrow S_0$ absorption band. It is already established in our previous work [25,26] that the coupling between S_1 state with the rest of the higher excited states occurs much beyond the energy range of the first electronic absorption band of MFBz, *o*-DFBz and *m*-DFBz molecules. The coupling strength of the relevant vibrational modes is also very weak [25, 26]. These findings explained the observed structure in the first absorption band of these molecules. Contrary to this, in case of PFBz occurrence of low-energy CIs between the S_1 and S_2 states (due to increased perfluoro effect) the first absorption band becomes structureless and diffuse [25,26]. The S_1-S_2 nonadiabatic coupling in PFBz is also much stronger compared to the other three molecules mentioned above [25,26]. However, in case of HFBz the present findings reveal that the energetic minimum of $S_1 - S_2$ CIs occurs at further lower energy compared to PFBz. As a result the seam of $S_1 - S_2$ CI is expected to be more readily accessible to the nuclear motion on the S_1 electronic state. Therefore, much profound effect on the spectral envelope of the first and second absorption bands of HFBz can be expected. In order to confirm this, we in the present study first construct various reduced dimensional models and examine the vibrational energy levels of each of these electronic states by excluding the PJT coupling with their neighbors. These results help us to understand the role of various vibrational modes and electronic states in the complex vibronic structures of HFBz. The final simulation of nuclear dynamics is, however, carried out by including all relevant couplings of the Hamiltonian and propagating wave packets using the MCTDH suite of programs [47–50] to elucidate the nonadiabatic coupling effects on the spectral envelopes. The theoretical results are finally compared with the available experimental absorption spectrum of HFBz [13].

The optical absorption spectrum of the uncoupled (without PJT coupling) nondegenerate S_1, S_3 and S_5 electronic states is shown in panel a, b and c of Fig. 6.4, respectively. According to the symmetry selection rule, only totally symmetric vibrational modes can have non-zero first-order (intrastate) coupling in these nondegenerate electronic states. We therefore considered both linear and quadratic coupling terms due to these modes in the nuclear dynamics study on these electronic states. The theoretical stick spectrum of the S_1 state (panel a of Fig. 6.4) is obtained by considering a vibrational basis consisting of 9 and 27 harmonic oscillator functions along ν_1 and ν_2 vibrational modes, respectively. The resulting secular matrix is diagonalized using 5000 Lanczos iterations. The theoretical stick spectrum is convoluted with a Lorentzian line shape function of 40 meV FWHM to generate the spectral envelope. The same convolution procedure is applied to all later stick data presented in this chapter. The vibronic structure of uncoupled S_1 electronic state (panel a) reveals peak spacings corresponding to the frequencies of ν_1 and ν_2 vibrations of $\sim$0.1328 and $\sim$0.0664 eV, respectively. The dominant progression is formed by the ν_2 vibrational mode. Similarly, the spectra of the S_3 and S_5 states presented in panels b and c are obtained by diagonalizing the secular matrix employing 5000 Lanczos iterations using 9 and 27 harmonic oscillator functions for S_3 and 10 and

40 harmonic oscillator functions for S_5 electronic state, respectively along the ν_1 and ν_2 vibrational modes. The vibrational mode ν_2 forms the dominant progression in both these electronic states. Peak spacings of ~ 0.0694 and ~ 0.0600 eV corresponding to the frequency of this mode can be extracted from the spectrum of the S_3 (panel b) and S_5 (panel c) electronic states, respectively. The vibrational mode ν_1 is very weakly excited in all these nondegenerate electronic states.

While the totally symmetric (a_{1g}) vibrational modes are coupled in first-order in the nondegenerate S_1, S_3 and S_5 states only, the JT active (e_{2g}) vibrational modes can have non-zero first-order coupling in the degenerate S_2 and S_4 states in addition. Therefore, all the a_{1g} and e_{2g} vibrational modes are considered to examine the nuclear dynamics in the latter two electronic states. We note that in absence of PJT and bilinear coupling terms, the Hamiltonian for the degenerate (S_2 and S_4) electronic state is separable in terms of the a_{1g} and e_{2g} vibrational modes. Therefore, in the dynamics study the partial spectrum for the a_{1g} and e_{2g} vibrational modes are calculated separately and finally convoluted to generate a composite vibronic band to describe the overall picture. The vibrational structure of the S_2 electronic manifold of HFBz is shown in Fig. 6.5. The partial spectra due to a_{1g} and e_{2g} vibrational modes and their composite are presented in panels a, b and c of Fig. 6.5, respectively. The stick spectra presented in Fig. 6.5 and all latter ones shown below are converged with respect to the size of the harmonic oscillator basis as well as number of Lanczos iterations. The dominant progression in the band of panel a is caused by the ν_2 vibrational mode. Peak spacing of $\sim$0.0647 eV corresponding to the frequency of the ν_2 vibrational mode can be estimated from the spectrum. Fundamental transition due to ν_{15}, ν_{16} and ν_{18} vibrational modes are observed in the partial spectrum of the degenerate e_{2g} vibrational modes shown in panel b. Lines are $\sim$0.1956, $\sim$0.0435 and $\sim$0.0376 eV spaced in energy and correspond to the frequency of the ν_{15}, ν_{16} and ν_{18} vibrational modes, respectively. The clumping of spectral lines under each peak and a huge increase of line density indicates strong JT coupling effects due to the vibrational modes ν_{15}, ν_{16} and ν_{18}, respectively. Such a coupling leads to the appearance of a long series of resonances corresponding to the vibrational motion on the lower JT sheet of the S_2 electronic manifold for energies below $\sim$5.6 eV. Similarly for energies above $\sim$5.6 eV, the upper sheet of S_2 electronic manifold plays a role. Nevertheless, the strong nonadiabatic effects mix the discrete vibrational levels of upper adiabatic sheet with the quasi-continuum levels of lower adiabatic sheet, and therefore, the nuclei undergo simultaneous transitions to both sheets of the JT split PES. The occurrence of higher energy maximum in the spectral envelope of Fig. 6.5(b) is due to metastable resonances of the upper adiabatic cone where as, the lower energy maximum arises from the lower adiabatic sheet. The broadening mechanism and the appearance of high energy peaks are just the strong nonadiabatic coupling effects characteristic for JT intersections [34, 37, 40]. These high energy peaks are referred to as Slonczewski resonances, and the evidence of these resonances was reported in the literature for several (E $\times$ e)-JT problems [61–63].

Similar spectra of the JT split S_4 electronic manifold of HFBz are shown in Figs. 6.6(a-c). The symmetric vibrational modes, ν_1, ν_2, and their combinations form the progressions (panel a) in this case also. The excitation strength of the ν_1 mode is $\sim$ 3

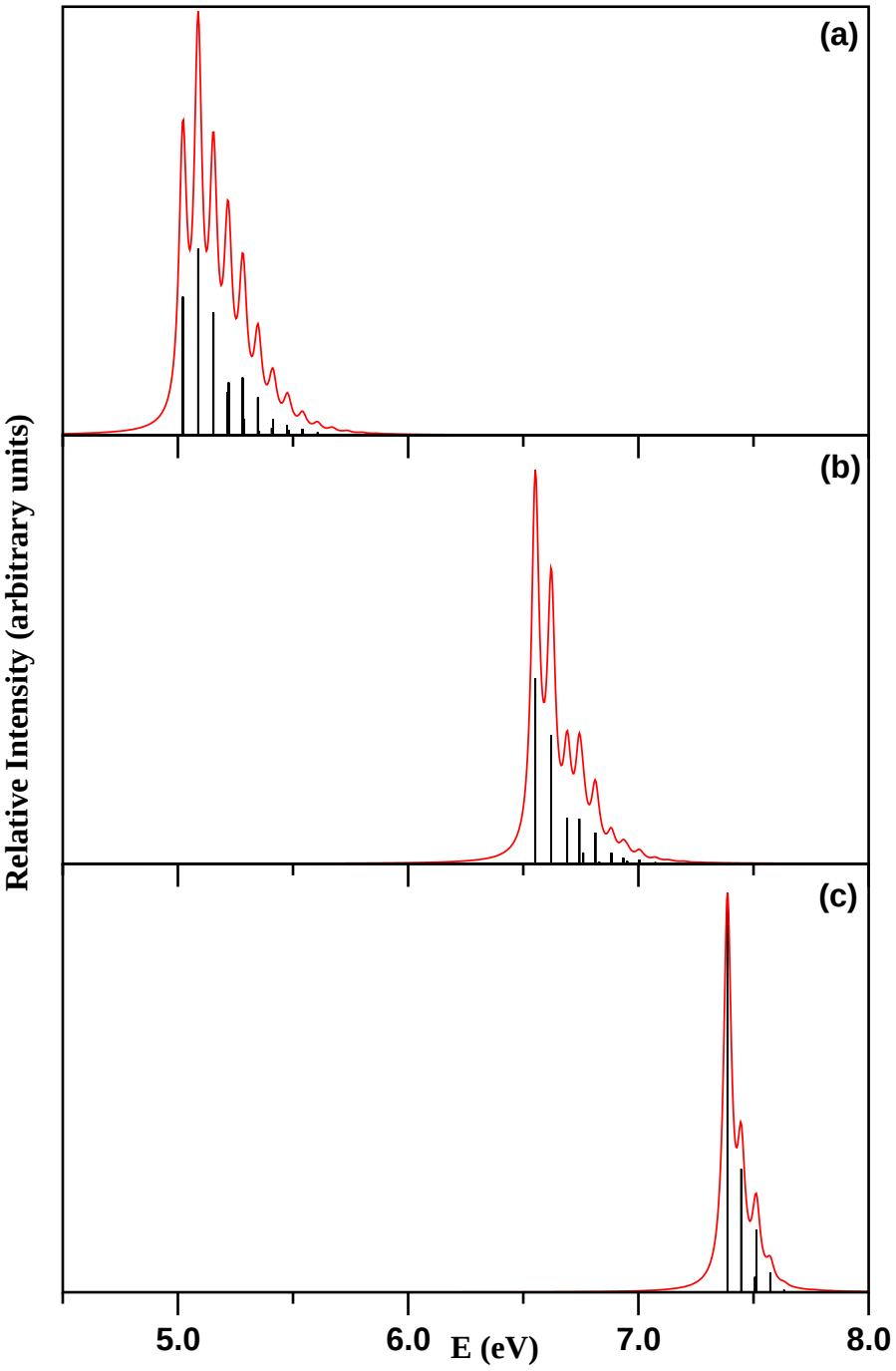

Figure 6.4: ${S_1}^1B_{2u} \leftarrow \mathrm{S}_0$ (panel a), ${S_3}^1B_{1u} \leftarrow \mathrm{S}_0$ (panel b) and ${S_5}^1A_{2u} \leftarrow \mathrm{S}_0$ (panel c) electronic absorption spectrum (excluding all interstate couplings) of HFBz. The above spectra are calculated with the symmetric vibrational modes ν_1 and ν_2 only. The relative intensity (in arbitrary units) is plotted as a function of the energy of the final electronic state. The zero of the energy corresponds to the equilibrium minimum of the electronic ground state (S_0) of HFBz. The theoretical stick spectrum in each panel is convoluted with a Lorentzian function of 40 meV FWHM to generate the corresponding spectral envelope.

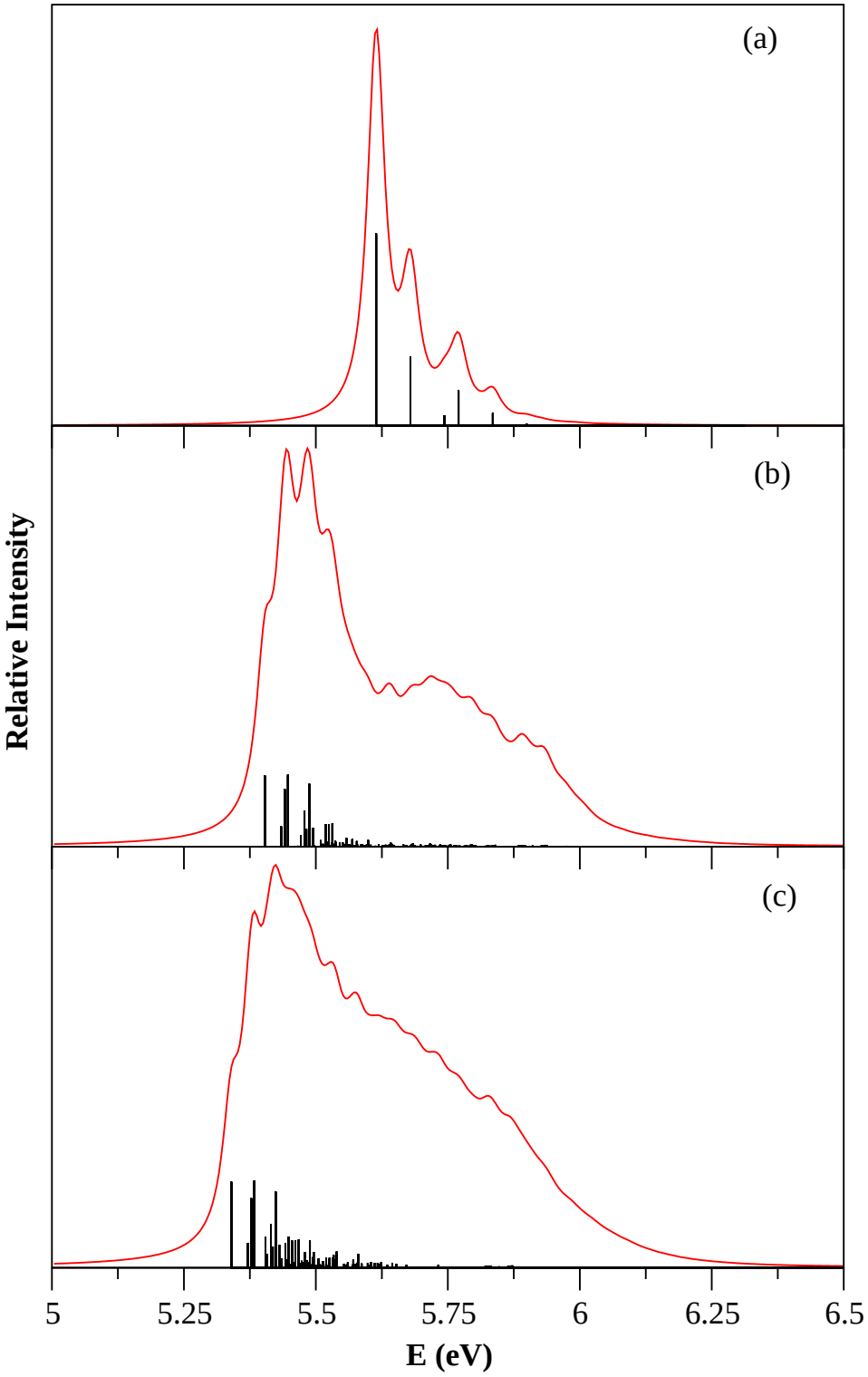

Figure 6.5: Same as in Fig. 6.4 for the $S_2\,^1E_{1g} \leftarrow S_0$ electronic transition in HFBz : (a) partial spectrum computed with the two totally symmetric a_{1g} vibrational modes ν_1 and ν_2, (b) partial spectrum computed with the four JT active degenerate e_{2g} vibrational modes ν_{15}-ν_{18}, and (c) the composite theoretical spectrum obtained by convoluting the above two partial spectra. The stick spectrum of panel c is multiplied by a factor of 3 for a better clarity.

times weaker than that of the ν_2 mode. The intense lines in panel a are ∼0.1874 and ∼0.0662 eV spaced relative to the band origin and correspond to the frequency of the ν_1 and ν_2 vibrational modes, respectively, in the S_4 state.

In contrast to the S_2 state spectrum of Fig. 6.5(a), the spectrum in Fig 6.6(a) exhibits an extended progression owing to a relatively larger coupling strength of ν_1 and ν_2 modes (cf. Table 6.3) in the S_4 state. On the other hand,the spectrum for the JT active e_{2g} vibrational modes for the S_2 state, shown in Fig. 6.5(b), exhibits much more complex structure compared to that for the S_4 state (cf. Fig. 6.6(b)). The complex energy level structure of Fig. 6.5(b) clearly reveals stronger JT coupling effects in the S_2 state and as a result the composite band of this state (panel c of Fig. 6.5) becomes highly diffuse and structureless. Since the JT effect in the S_4 state is extremely weak, the composite band structure of this state [cf. Fig. 6.6(c)] essentially resembles the symmetric mode spectrum of Fig. 6.6(a).

While the spectrum of the individual states presented above contains rich information on the excitation of various vibrational modes, their overall structure is far from the one recorded in the experiment [12, 13, 19–22]. Apart from the JT coupling within the degenerate electronic states, several other interstate couplings (cf. Table 6.4) are important and need to be considered to arrive at a satisfying agreement with the experiment [12, 13, 19–22]. The important interstate couplings are discussed in Sec. 6.4 in terms of the topological characteristics of the adiabatic potential energy surfaces. The dynamical consequences of these couplings are examined and discussed in the following. Twenty three relevant vibrational modes and all relevant couplings of the vibronic Hamiltonian of Eqs. (6.2-6.3) are considered for this exercise. Such a consideration leads to a huge increase of the dimension of the vibronic secular matrix and a diagonalization of it is numerically impossible with the available computer hardware. We therefore use the Heidelberg MCTDH suite of program [47–50], and propagate WPs to calculate the broad band spectrum considering all the required degrees of freedom. The numerical details of these calculations are given in Table 6.6. We note that, it was necessary to adjust the vertical excitation energies within the error limit of EOM-CCSD data to reproduce the adiabatic excitation energies at their experimental values [13, 20, 21]. Apart from this, no other parameters are adjusted in our theoretical calculations. The adjusted vertical excitation energies are given in Table 6.5.

Seven calculations are carried out by initially preparing the WP separately on each component of the S_1-S_2- S_3-S_4-S_5 electronic manifold. The WP in each case is propagated for 200 *fs*. Numerically converged spectra for the S_1 and S_2 states obtained from these calculations are shown in panel c of Fig. 6.7 along with the experimental results in panel a and b reproduced from Ref. [13] and Ref. [20], respectively. The time autocorrelation function is damped with an exponential function, ($e^{-\frac{t}{\tau}}$, with τ_r= 33 fs), prior to its Fourier transformation to calculate the spectrum. Such a damping is equivalent to a convolution of the energy spectrum with a Lorentzian lineshape function of 20 meV FWHM. It can be seen that the theoretical result of panel c is in very good accord with the old and recent experiments [13, 20, 21]. The structured absorption band of the uncoupled S_1 state (cf. Fig. 6.4(a)) becomes essentially structureless upon considering its coupling with the other states. The PJT coupling of S_1 state with S_2 along the ν_{19}

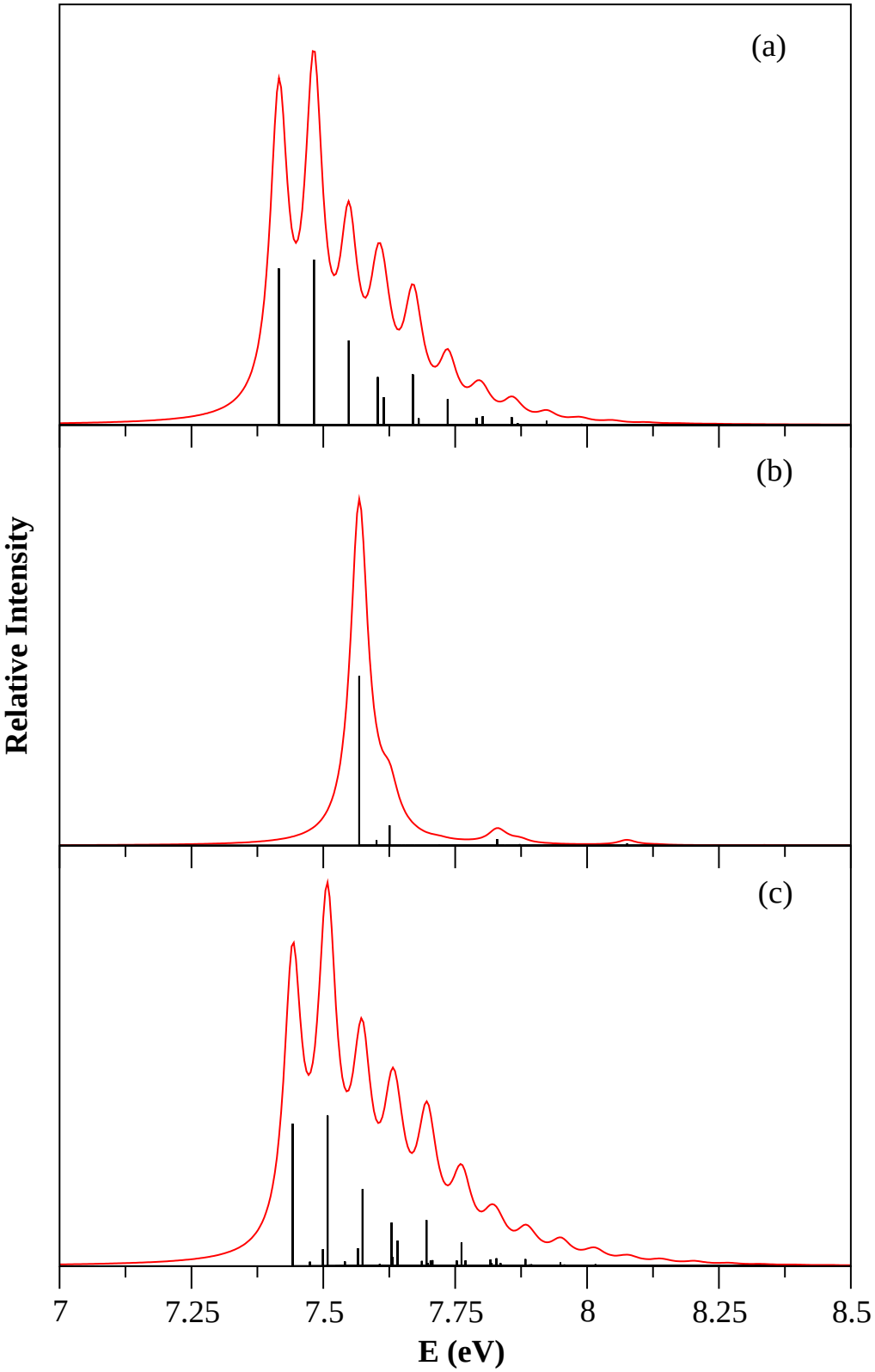

Figure 6.6: Same as in Fig.6.4 for the $S_4\,^1E_{1u} \leftarrow S_0$ electronic transition in HFBz

and ν_{20} vibrational modes [cf. Table 6.4] is very strong. As discussed in Sec. 6.4 the energetic minimum of the S_1 and S_2 CIs occurs at lower energy and the seam of CIs is therefore readily accessible to the nuclear motion on the S_1 electronic state. The intersections of S_1 state with S_3, S_4 and S_5 occur at much higher energies and do not have any impact on the nuclear dynamics on the S_1 state.

The broad band above $\sim$ 5 eV in Fig. 6.7 represents the vibronic structure of the JT active S_2 state. It can be seen from the spectra plotted in panel b and c of Fig. 6.5 for the S_2 state that the JT effect itself is very strong within this state, as a result a bimodal vibronic band is obtained for this electronic state. The S_1-S_2 PJT coupling further broadens the band structure of this state. The energetic minimum of the S_1-S_2 curve crossings is very close to the minimum of the JT intersections within the S_2 electronic state (cf. Sec. 6.4). The two peaks in the bimodal spectral profile arise from the two JT split adiabatic electronic sheets of the S_2 state. These peaks located at $\sim$ 5.35 and $\sim$ 5.75 eV and are in excellent accord with their experimental values [cf. Table 6.5 for a detailed comparison].

The third and fourth absorption bands of HFBz obtained with the full Hamiltonian of Eq. 6.3 are shown in panel b of Fig. 6.8. These bands are formed by the S_3, S_4 and S_5 electronic states of HFBz. All these states are of $\pi\pi^*$ type (cf. Fig.6.1). The corresponding experimental results are reproduced from Ref. [13] and shown in panel a of Fig. 6.8. The two curves in panel a emerged from a decomposition of experimental spectrum [13]. This was done to eliminate the overlapping components and to correctly estimate the oscillator strengths of the two curves of $^1B_{1u}$ and $^1E_{1u}$ Bz parentage [13]. It can be seen from Fig. 6.8 that theoretical results are in satisfactory agreement with the low-resolution experimental data. In case of Bz the signature of the $^1A_{2u}$ state was not seen distinctly as it was buried within the spectral envelope of the JT active E_{1u} state. In case of HFBz the $^1A_{2u}$ state appears vertically at an energy above the JT active $^1E_{1u}$ state (cf. Fig. 6.1). As a result the distinct feature seen at an energy beyond $\sim$ 7.5 eV appears due to the $^1A_{2u}$ electronic state of HFBz (cf. Fig. 6.8). This feature was tentatively assigned at $\sim$7.7 eV in the experimental results (cf. Table 6.5) originating from this state and the present findings confirms this assignment. It is important to note that we carried out various two-coupled states calculations in order to confirm the assignment of the peaks appeared in the broad envelopes of Fig. 6.8(b).

At this point, it is worthwhile to compare the present theoretical results to those available in the literature. The lowering of the $\pi\sigma^*$ state energy with increasing fluorination have been predicted by Zgierski *et al.* [19] and by Studzinski *et al.* [22] through TDDFT calculations. Their results show that this $\pi\sigma^*$ state becomes the lowest excited state in case of HFBz at the equilibrium geometry of the S_0 state. By comparing the features observed in the fluorescence and absorption spectra of jet cooled PFBz and HFBz with other FBz derivatives with less number of fluorine atoms Zgierski *et al.* concluded that the S_1 state of the former molecules deserves a $\pi\sigma^*$ assignment [19]. This assignment is also supported by performing TDDFT calculations by Studzinski *et al.* [22]. However, this assignment differs from that of Motch *et al.* [20] and Holland *et al.* [21] who established with the aid of a combined experimental and computational study that the LUMO of HFBz is of π^* character. The present findings reveal that the lowest $\pi\sigma^*$ state

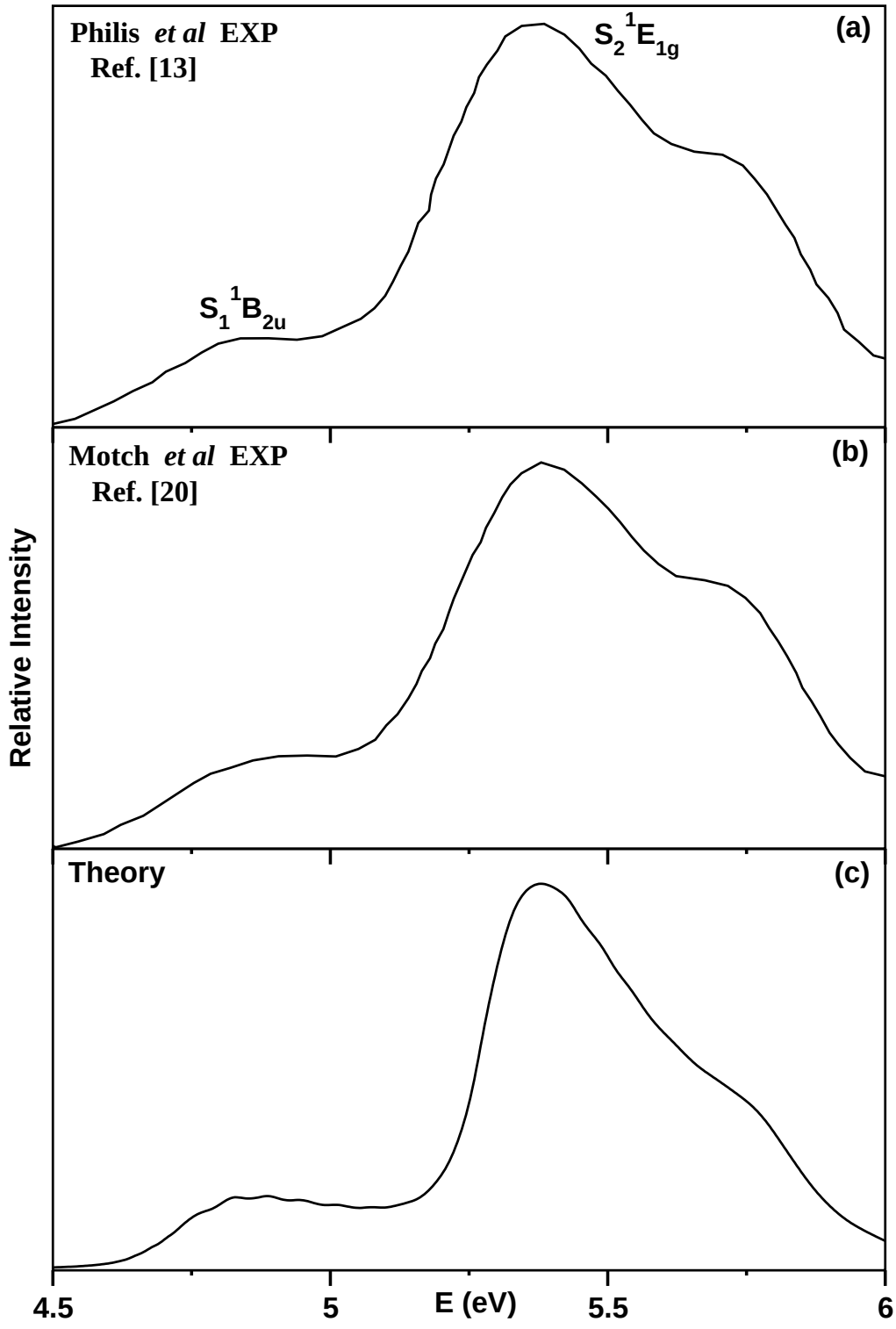

Figure 6.7: Vibronic bands of the S_1-S_2 states of HFBz calculated using seven states and twenty three vibrational modes using MCTDH algorithm with a damping time of 33 *fs*. The experimental [13, 20] and theoretical results are shown in panel a, b and c, respectively. The intensity (in arbitrary unit) is plotted along the energy (relative to minimum of the $^1A_{1g}$ state of HFBz) of the final vibronic states.

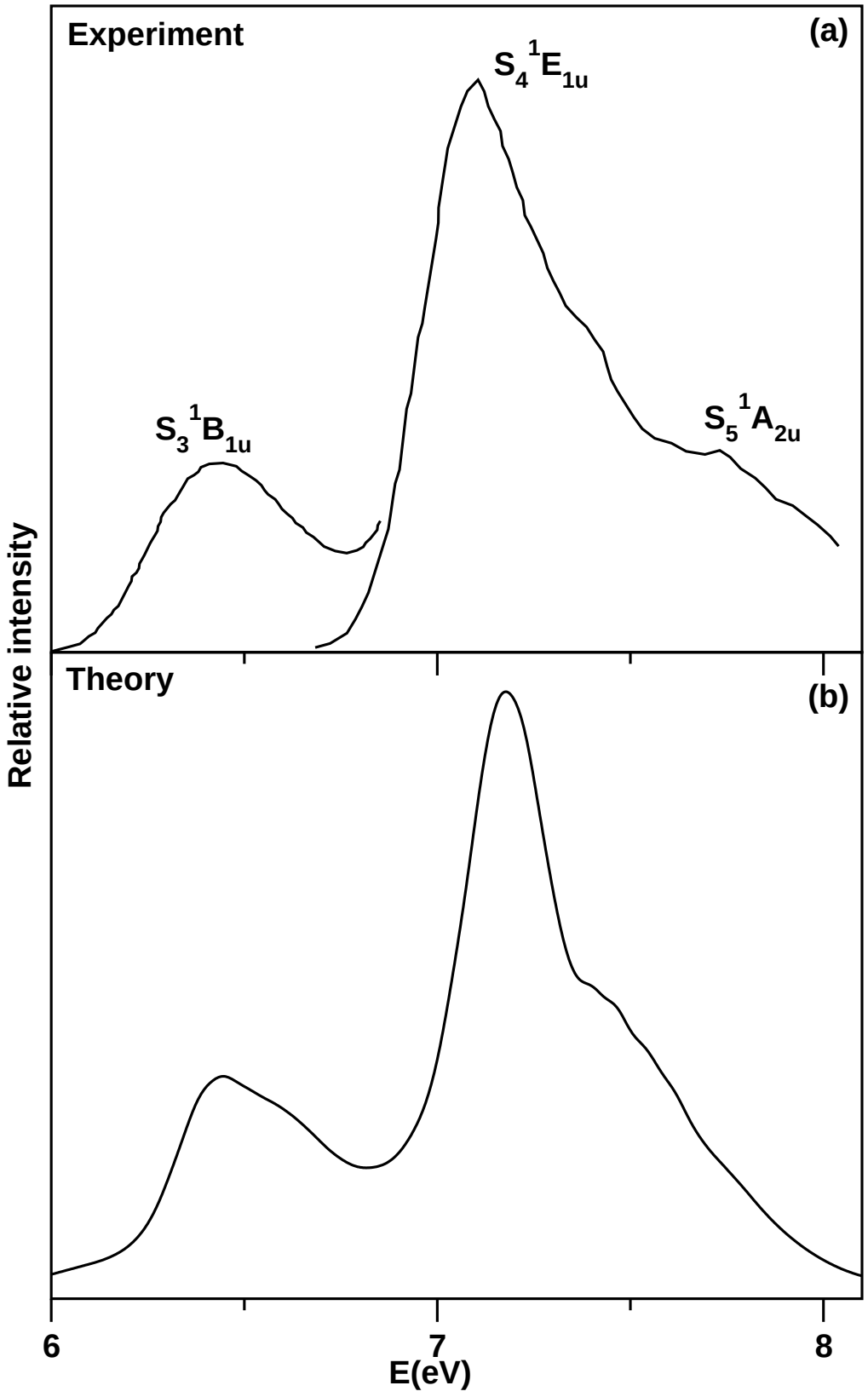

Figure 6.8: Same as Fig. 6.7, for S_3-S_4-S_5 electronic states of HFBz with a damping time of 12 *fs*.

Table 6.6: Normal mode combinations, sizes of the primitive and the single particle basis used in the wave packet propagation within the MCTDH framework in the seven coupled electronic manifold using the complete vibronic Hamiltonian of Eq. (6.3). Second column denotes the vibrational DOF which are combined to particles. Third column gives the number of primitive basis functions for each DOF. Fourth column gives the number of SPFs for each electronic state.

Molecule	Normal modes	Primitive basis	SPF basis
HFBz	(ν_1, ν_{18y}, ν_{20y}, ν_{11y})	(8, 6, 10, 4, 6)	[8,25,25,6,6,6,6]
	(ν_2, ν_{16x}, ν_{20x}, ν_{11x}, ν_{12y})	(10, 5, 10, 4, 6)	[9,6,6,6,12,12,6]
	(ν_{18x}, ν_{17y}, ν_{19x}, ν_{14x}, ν_7)	(6, 8, 10, 4, 6)	[18,18,18,25,6,6,18]
	(ν_{17x}, ν_{16y}, ν_{19y}, ν_{14y}, ν_8)	(8, 5, 10, 4, 8)	[18,8,8,18,9,9,18]
	(ν_{15x}, ν_{15y}, ν_3, ν_{12x})	(8, 8, 4, 6)	[8,6,6,6,6,6,6]

becomes S_2 in HFBz and the assignments of the structure appearing in photoabsorption spectrum between ∼4.5 and ∼6 eV in the present study [25, 26] are consistent with the findings of Philis *et al.* [13], Motch *et al.* [20] and Holland *et al.* [21]. It is intriguing to note that the age old experimental results of Refs. [12, 13] are in very good agreement with those obtained in the modern experiments [20, 21] and it can be seen form Fig. 6.7 that our theoretical results are in perfect accord with the findings from all these experiments. In order to reconfirm, we carried out calculations of VEEs using five other different wavefunction based approaches (as possible for this large system) and also using the TDDFT method. The magnitude of the VEEs differ in each calculations but they confirm that S_1 and S_2 states of HFBz is of $\pi\pi^*$ and $\pi\sigma^*$ character, respectively. The TDDFT calculations using the G03 program package [52] indeed gave a reverse energetic ordering of these two states as reported in Refs. [19, 22]. To save space and brevity we do not include here all the test results obtained by us using different electronic structure methods. Instead, we note that the electronic structure results employed in this work offers the best agreement with the experiment for this "large"molecular system. The detailed analysis carried out here along with the literature results (both theory and experiments, see Table 6.5) confirm that the S_2 state is $\pi\sigma^*$ in HFBz at the equilibrium geometry of the S_0 state. This state comes down in energy with increasing fluorination and forms the lowest energy CIs with the S_1 state in HFBz. Further support to the above assignment of the state order arise from a recent experimental and computation study on perfluorinated oligophenylenes. For these higher homologues of HFBz the S_1 state is found to be of $\pi\pi^*$ type [64].

Temps *et al.* have studied ultrafast nonradiative dynamics of electronically excited HFBz [22]. These authors arrived at the same results as reported by Zgierski *et al.* [19]. The S_1 state was found to be of $\pi\sigma^*$ type ($^1E_{1g}$ symmetry) through TDDFT calculations [22]. Four peaks were reported in the optical absorption spectrum of HFBz recorded by Temps *et al.* (cf. Fig. 1 of Ref. [22]) in the ∼ 210-280 nm wavelength region. Apparently, the weakest one appearing at the longest wavelength was assigned to the $S_1(^1E_{1g}) \leftarrow S_0(^1A_{1g})$ transition. This transition is dipole forbidden. The weak absorption and low-

quantum yield of fluorescence of this optically dark state is attributed to its strong nonadiabatic coupling with the $^1B_{2u}(S_2)$ state of $\pi\pi^*$ origin. The next three peaks were assigned to the $S_2(^1B_{2u}) \leftarrow S_0(^1A_{1g})$, $S_3(^1B_{1u}) \leftarrow S_0(^1A_{1g})$ and $S_4(^1E_{1u}) \leftarrow S_0(^1A_{1g})$ transition, respectively. The present electronic structure and dynamics results reported in Figs. 6.1, 6.5 and 6.7 differ considerably from this assignment. We reiterate that the S_1 state is a $\pi\pi^*$ state and NOT a $\pi\sigma^*$ state at the equilibrium configuration the S_0 state of HFBz (cf. Fig. 6.1). A wave function based approach of quantum chemical calculations, therefore predicted that the S_1 state is of $^1B_{2u}$ symmetry. Unlike in Ref. [22], the three peaks observed in the spectrum plotted in the panel c of Fig. 6.7 are assigned to a transition to the $^1B_{2u}(S_1)$ and $^1E_{1g}(S_2)$ electronic states of HFBz. The bimodal structure of the latter band arises due to strong JT splitting of 1^1E_{1g} state along the vibrational modes of e_{2g} symmetry. These assignments are also consistent with the experimental results of Philis *et al.* [13], Motch *et al.* [20] and Holland *et al.* [21]. The splitting between the two maxima of the theoretical spectrum of ∼0.40 eV of the $S_2{}^1E_{1g}$ [*cf.* Fig. 6.7(c)] state compares well with it's experimental value [13].

6.6 Internal conversion dynamics

In order to understand the impact of complex nonadiabatic coupling on the dynamics of the coupled S_1-S_2-S_3-S_4-S_5 excited electronic states, the time-dependence of diabatic electronic populations is plotted in Fig. 6.9. These electronic populations are obtained by initially locating the WP on the S_1 state, one component of the JT split S_2 state, the S_3 state, one component of the JT split S_4 state and the S_5 state and shown in Fig. 6.9, respectively. It can be seen from panel a of Fig. 6.9 that the electronic population transfer occurs only to the S_2 state when the WP is initially prepared on the S_1 state. It was found in our previous work [26] that the energetic minimum of S_1-S_2 CIs decreases gradually from MFBz to PFBz due to the lowering of S_2 state energy by the perfluoro effect. The present calculations reveal that the minimum of the S_1-S_2 CIs in HFBz occurs at ∼5.51 eV, which is even lower in energy compared to that of PFBz occurring at ∼ 6.92 eV (see Table VIII of Ref. [25]). Therefore, the S_1-S_2 CI is more readily accessible to the WP moving on the S_1 state of HFBz when compared to PFBz. The initial decay of the population relates to a nonradiative internal conversion rate of ∼ 153 *fs* of the S_1 state. The femtosecond time-resolved experiment of Temps *et al.* [22] predicts a decay rate of ∼ 172 fs of this initially excited state. We reiterate that this state is designated as $\pi\sigma^*$ in contrast to our designation as $\pi\pi^*$.

The CIs of S_1 state with S_3, S_4 and S_5 states occur at high energies and these are not accessible to the WP prepared on the S_1 state as clearly indicated by the population diagram shown in Fig. 6.9. It is discussed above that the S_1-S_2 CIs are the bottleneck underlying the broadening of the $S_1 \leftarrow S_0$ absorption band in HFBz. The WP initially prepared on the S_2 state moves very fast to the S_1 state (panel b). A nonradiative decay rate of ∼22 *fs* can be estimated from the population curve of S_2 state given in panel b. It is to be noted from the population diagram of Fig. 6.9, that the population of the second component of the JT split S_2 state also grows in time. However, the population

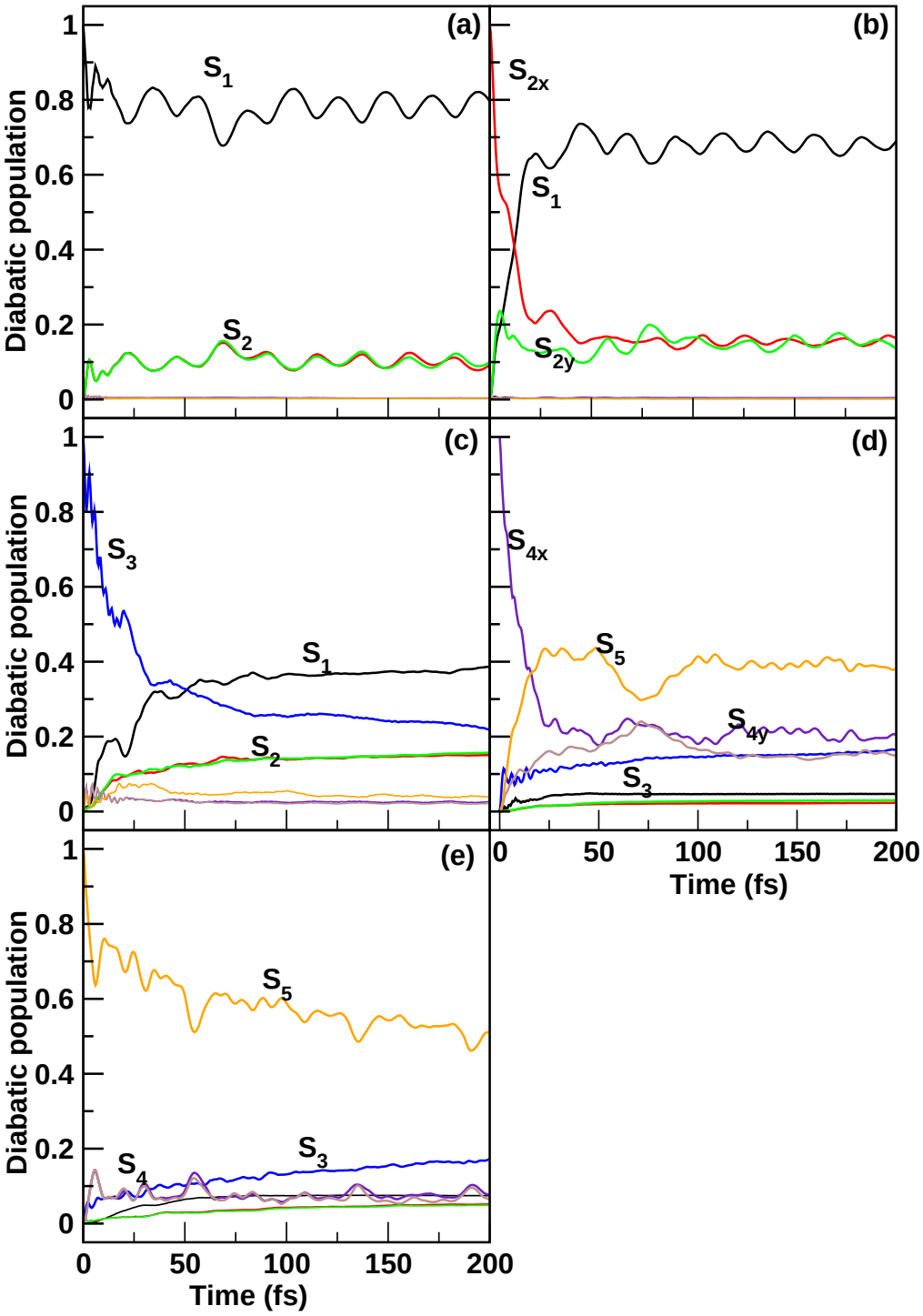

Figure 6.9: Time-dependence of diabatic electronic populations in the S_1-S_2-S_3-S_4-S_5 coupled state nuclear dynamics of HFBz. The results obtained by initially locating the WP on the S_1 state, one component of the JT split S_2 state, S_3 state, one component of the JT split S_4 state and S_5 state are shown in panel a-e, respectively.

growth of the latter state is much slower than that of the S_1 state. This indicates that the S_1-S_2 PJT coupling is much stronger than the JT coupling within the S_2 electronic manifold. The electronic structure data given in Tables 6.3 and 6.4 are in accord with these findings. Therefore it is clear that much of the broadening of the spectral envelope of the S_1 and S_2 state is caused by the strong S_1-S_2 PJT coupling particularly, along the ν_{20} vibrational mode of e_{2u} symmetry.

The electron population dynamics becomes more complex and involved when the WP is initially prepared either on the S_3 (panel c), S_4 (panel d) or S_5 (panel e) electronic state. In the former case most of the population transfers to S_1 state via two consecutive low-energy S_3-S_2 and S_2-S_1 CIs. Similarly, when the WP is prepared on the S_4 state the internal conversion to the S_3 and S_5 states occurs due to strong S_4-S_3 and S_4-S_5 interstate coupling (cf. Table 6.4). The initial sharp decay of the population of the S_3 and S_4 states in panels c and d relates to the nonradiative decay rate of $\sim$67 and $\sim$28 *fs* of these states, respectively. When the WP is prepared on the S_5 state, the population transfers to the S_3 and S_4 states only. A nonradiative decay rate of $\sim$110 *fs* is found for this state.

A few remarks are in order at this point. The electronic structure and quantum dynamics results presented above revealed excellent agreement with the experimental findings. The detailed comparative account on the energetic location of the bands presented in Table 6.5 reveals that the present theoretical results are in perfect accord with the experimental findings of Frueholz *et al.* [11,12], Philis *et al.* [13], Motch *et al.* [20] and Holland *et al.* [21]. Apart from a reverse energetic ordering of the two lowest excited electronic states of HFBz the other observations made in the experiment of Ref. [19, 22] can very well be understood from the present theoretical results. It is shown that the PJT coupling between the S_1 and S_2 states of HFBz is much stronger than the JT coupling within the S_2 electronic state. It is discussed in section 6.4 that the energetic minimum of the S_1-S_2 intersection is near degenerate to the minimum of the S_2 state. This energetic minimum of the S_2 state occurs at a displaced geometry at Q_1=-0.79, Q_2=0.66, Q_{15x}=-0.94, Q_{16x}=-0.41, Q_{17x}=-1.99, Q_{18x}=-1.21, Q_{19x}=0.0, Q_{20x}=0.0 from the original vertical configuration (at Q=0). It can be seen that $\sim$ 20 % of the electronic population flows to the S_2 state (cf. panel a of Fig.6.9) upon an initial Franck-Condon transition to the S_1 ($\pi\pi^*$) state. A part of this 20% population trapped in the vicinity of the minimum of the S_2 ($\pi\sigma^*$) state gives rise to fluorescence emission. Since this part is expected to be quite small, extremely low quantum yield of fluorescence is obtained in the experimental measurements [19]. Also, since this emission occurs from a geometry away from the vertical configuration (as stated above), overlap of the absorption and emission band is not observed [19]. Strong S_1-S_2 nonadiabatic interaction causes a mixing of the energetically low-lying vibronic levels of the S_2 state with the continuum levels of the S_1 state and gives rise to a large spectral width. The relatively weaker JT coupling within the S_2 state also contributes to the spectral broadening as discussed in Sec 6.5 above.

6.7 summary

A detailed theoretical account of multi-mode JT and PJT interactions in five lowest excited singlet electronic states of HFBz is presented in this contribution. Extensive electronic structure calculations are performed to develop a model diabatic vibronic coupling Hamiltonian (Eqs. 6.2-6.6b), and first-principles dynamics calculations are carried out both via time-independent and time-dependent quantum mechanical methods. The calculated adiabatic potential energies of five electronic states are parametrized to establish the diabatic vibronic Hamiltonian. Using the constructed Hamiltonian the nuclear dynamics is systematically studied to reveal impact of electronic nonadiabatic coupling on the dynamics. The electronic structure data reveal multiple CIs among these excited electronic states of HFBz. The theoretical findings are found to be in good accord with the available experimental results.

Several issues regarding the complex vibronic dynamics of HFBz (as compared to Bz) are addressed and resolved in this chapter. The major findings are the following.
1. The S_2 state of HFBz is JT active, two $\pi\sigma^*$ states are energetically degenerate in this case. This is not the case for any other fluoro derivatives of Bz with number of fluorine atoms less than 6.
2. Some of the earlier works [19, 22] predicted that the S_1 state is of $\pi\sigma^*$ type in PFBz and HFBz. This assignment has been found to be incorrect in the present study. The S_1 state is of $\pi\pi^*$ type for all FBz molecules. This result is also in accord with the recent findings in the literature [21].
3. The present assignment of the peaks in the photoabsorption spectrum of HFBz is in agreement with the experimental results of Philis *et al.* [13] but is in contradiction with that of Temps *et al.* [22].
4. The structureless S_1 band of HFBz originates from energetically low-lying CIs of the S_1 and S_2 states and very strong PJT coupling among them.
5. The bimodal shape of the second photoabsorption band originates from the orbitally degenerate JT active $^1E_{1g}$ electronic state of HFBz. The energetic location of these two peaks is in good agreement with the experimental results of Philis *et al.* [13]. The JT coupling is strong in this electronic state which causes a bimodal shape of the absorption profile, the PJT coupling of this state with S_1 is even stronger which causes this bimodal spectral profile structureless. We note that this state is optically dark for a transition from the electronic ground state of HFBz. The absorption profile of this state seen in the experiment is due to its vibronic coupling with the optically bright S_1 state.
6. The JT coupling in the $^1E_{1u}$ electronic state is far weaker than in the $^1E_{1g}$ state of HFBz. The $^1E_{1g}$-$^1E_{1u}$ PJT coupling is symmetry allowed and there exist vibrational modes of appropriate symmetry to cause this coupling. The symmetry invariance of $^1E_{1g}$- $^1E_{1u}$ coupling matrix is studied and the relative phases of the coupling elements are derived. However, thorough analysis of the electronic structure data reveal negligible coupling among these degenerate electronic states.
7. The third and forth absorption bands of HFBz are formed by three $\pi\pi^*$ type of orbitals of $^1B_{1u}$, $^1E_{1u}$ and $^1A_{2u}$ symmetry. Unlike in case of Bz, the signature of the $^1A_{2u}$ state is clearly seen in the absorption spectrum of HFBz. This state appears at

$\sim$ 7.7 eV in the experimental spectrum [13] and is in good accord with our theoretical results.
8. Nonradiative decay rate of $\sim$ 153 fs and $\sim$ 22 fs is found for the S_1 and S_2 state, respectively. Electronic population transfer occurs to the S_1 state via S_3-S_2 and S_3-S_1 CIs when the S_3 state is initially populated. Likewise, nonradiative electron population transfer occurs to the S_3, S_5 and S_3, S_4 states when the S_4 and S_5 states are initially populated, respectively. These nonradiative transfer of electron populations relate to decay rate of $\sim$ 67, 28 and 110 fs, respectively, of the S_3, S_4 and S_5 electronic states of HFBz.

6.8 Appendix: Symmetry analysis of $E_{1g} - E_{1u}$ JT and PJT Hamiltonian

The symmetry invariance of the vibronic Hamiltonian of Bz^+ discussed by Köppel and coworkers has been found to be applicable in case of HFBz also as both the systems belong to D_{6h} symmetry point group. In this appendix we examine the symmetry invariance of the $E_{1g} - E_{1u}$ PJT coupling block of the vibronic Hamiltonian of Eq. 6.3b. Since HFBz belongs to same D_{6h} symmetry point group as Bz^+, the JT coupling matrix derived for the E_{1g} and E_{1u} states in Ref. [35] is applicable to those states of HFBz also. The D_{6h} symmetry point group can be represented as $D_{6h} = D_6 \otimes i$; Where i represents the inversion operation. Like Bz^+ the latter operation is trivial for HFBz also. The principal rotation axis C_ϕ can be 2, 3 and 6 fold. The other symmetry operations are E, C_2' and C_2''. It is stated in the introduction that the symmetry rule allows the vibrational modes of e_{2u}, a_{2u} and a_{1u} to be PJT active in first-order in the $E_{1g} - E_{1u}$ coupled electronic manifold. Considering only the linear coupling terms the following analysis can be made.

A coupled Hamiltonian in the E_{1g} and E_{1u} electronic function spaces can be represented in terms of the electronic projection operators. Let the kets $|x_1\rangle$, $|y_1\rangle$ and $|x_2\rangle$, $|y_2\rangle$ and the corresponding bras represent the first and second rows/columns of the E_{1g} and E_{1u} representation matrices as given in Ref. [35]. Let us also denote the components of the degenerate vibrational modes by Q_x and Q_y. The following transformations hold.

First we will derive the vibronic Hamiltonian for JT active E_{1g} and E_{1u} electronic states.

$$\begin{aligned}
[|x_1\rangle\langle x_1| - |y_1\rangle\langle y_1|] \xrightarrow{C_\phi} & [cos^2(\phi) - sin^2(\phi)][|x_1\rangle\langle x_1| - |y_1\rangle\langle y_1|] \\
& +(2cos(\phi)sin(\phi))[|x_1\rangle\langle x_1| + |y_1\rangle\langle y_1|] \\
= & \; cos(2\phi)[|x_1\rangle\langle x_1| - |y_1\rangle\langle y_1|] \\
& +sin(2\phi)[|x_1\rangle\langle y_1| + |y_1\rangle\langle x_1|] \qquad \text{(A1)}
\end{aligned}$$

$$\begin{aligned} |x_1\rangle\langle y_1| + |y_1\rangle\langle x_1| &\xrightarrow{C_\phi} -2cos(\phi)sin(\phi)[|x_1\rangle\langle x_1| - |y_1\rangle\langle y_1|] \\ &\quad +(cos^2(\phi) - sin^2(\phi))[|x_1\rangle\langle y_1| - |y_1\rangle\langle x_1|] \\ &= -sin(2\phi)[|x_1\rangle\langle x_1| - |y_1\rangle\langle y_1|] \\ &\quad +cos(2\phi)[|x_1\rangle\langle y_1| + |y_1\rangle\langle x_1|] \end{aligned} \tag{A2}$$

From Eq. (A1) and Eq. (A2),

$$\begin{aligned} \begin{bmatrix} |x_1\rangle\langle x_1| - |y_1\rangle\langle y_1| \\ |x_1\rangle\langle y_1| + |y_1\rangle\langle x_1| \end{bmatrix} &\xrightarrow{C_\phi} \begin{bmatrix} cos(2\phi) & sin(2\phi) \\ -sin(2\phi) & cos(2\phi) \end{bmatrix} \begin{bmatrix} |x_1\rangle\langle x_1| - |y_1\rangle\langle y_1| \\ |x_1\rangle\langle y_1| + |y_1\rangle\langle x_1| \end{bmatrix} \\ &= Q_x[|x_1\rangle\langle x_1| - |y_1\rangle\langle y_1|] + Q_y[|x_1\rangle\langle y_1| + |y_1\rangle\langle x_1|] \end{aligned}$$

$Q_x[|x_1\rangle\langle x_1| - |y_1\rangle\langle y_1|] + Q_y[|x_1\rangle\langle y_1| + |y_1\rangle\langle x_1|]$, is invariant with respect to C_ϕ. Where Q_x and Q_y represent the x and y components of either e_{2g} or e_{2u} mode. Under inversion operator ($|x_1\rangle$, $|y_1\rangle$) and (Q_x, Q_y) transform as ($|x_1\rangle$, $|y_1\rangle$) and ($\pm Q_x$, $\pm Q_y$). To make the function $Q_x[|x_1\rangle\langle x_1| - |y_1\rangle\langle y_1|] + Q_y[|x_1\rangle\langle y_1| + |y_1\rangle\langle x_1|]$ invariant with respect to inversion, (Q_x, Q_y) should transform as (Q_x, Q_y) and hence the normal mode is a gerade e_{2g} representation. Similarly, this function can be shown to invariant with respect to the operations C_2' and C_2''.

Considering the symmetry invariance with respect to the operations given above, the E_{1g} JT coupling matrix for the e_{2g} vibrational mode is given by

$$\mathcal{H}^{JT}_{e_{2g}} = \begin{pmatrix} \lambda Q_x & \lambda Q_y \\ \lambda Q_y & -\lambda Q_x \end{pmatrix}$$

$$\begin{aligned} |x_1\rangle\langle x_1| + |y_1\rangle\langle y_1| &\xrightarrow{C_\phi} [cos^2(\phi) + sin^2(\phi)][|x_1\rangle\langle x_1| + |y_1\rangle\langle y_1|] \\ &= [|x_1\rangle\langle x_1| + |y_1\rangle\langle y_1|] \end{aligned} \tag{A3}$$

$$\begin{aligned} |x_1\rangle\langle y_1| - |y_1\rangle\langle x_1| &\xrightarrow{C_\phi} [cos^2(\phi) + sin^2(\phi)][|x_1\rangle\langle y_1| - |y_1\rangle\langle x_1|] \\ &= [|x_1\rangle\langle y_1| - |y_1\rangle\langle x_1|] \end{aligned} \tag{A4}$$

It can be proved that $Q_{a_{1g}}[|x_1\rangle\langle x_1| + |y_1\rangle\langle y_1|]$ and $Q_{a_{1u}}[|x_1\rangle\langle y_1| - |y_1\rangle\langle x_1|]$ are invariant with respect to all symmetry operations of D_6 point group. The E_{1g} JT coupling matrix for the a_{1g} and a_{1u} vibrational modes is given by

$$\mathcal{H}^{JT}_{a_{1g}\&a_{1u}} = \begin{pmatrix} \kappa Q_{a_{1g}} & \beta Q_{a_{1u}} \\ -\beta Q_{a_{1u}} & \kappa Q_{a_{1g}} \end{pmatrix}$$

The hermitian property of Hamiltonian requires

$$\begin{aligned}
\mathcal{H}_{12} &= \mathcal{H}_{21}^{*} \\
\beta Q_{a_{1u}} &= (-\beta Q_{a_{1u}})^{*} \\
\beta Q_{a_{1u}} &= -\beta Q_{a_{1u}} \text{ since the Hamiltonian is real} \\
2\beta Q_{a_{1u}} &= 0 \\
\beta &= 0 \text{ since } Q_{a_{1u}} \neq 0
\end{aligned}$$

Similarly the JT hamiltonian for E_{1u} can also be deduced from the symmetry properties. Now we proceed to deduce the E_{1g}-E_{1u} PJT coupling matrix.

$$\begin{aligned}
[|x_1\rangle\langle x_2| - |y_1\rangle\langle y_2|] \xrightarrow{C_\phi} & [cos^2(\phi) - sin^2(\phi)][|x_1\rangle\langle x_2| - |y_1\rangle\langle y_2|] \\
& +(2cos(\phi)sin(\phi))[|x_1\rangle\langle x_2| + |y_1\rangle\langle y_2|] \\
= & \; cos(2\phi)[|x_1\rangle\langle x_2| - |y_1\rangle\langle y_2|] \\
& +sin(2\phi)[|x_1\rangle\langle y_2| + |y_1\rangle\langle x_2|] \qquad \text{(A5)}
\end{aligned}$$

$$\begin{aligned}
|x_1\rangle\langle y_2| + |y_1\rangle\langle x_2| \xrightarrow{C_\phi} & -2cos(\phi)sin(\phi)[|x_1\rangle\langle x_2| - |y_1\rangle\langle y_2|] \\
& +(cos^2(\phi) - sin^2(\phi))[|x_1\rangle\langle y_2| - |y_1\rangle\langle x_2|] \\
= & -sin(2\phi)[|x_1\rangle\langle x_2| - |y_1\rangle\langle y_2|] \\
& +cos(2\phi)[|x_1\rangle\langle y_2| + |y_1\rangle\langle x_2|] \qquad \text{(A6)}
\end{aligned}$$

From Eq. (A5) and Eq. (A6),

$$\begin{aligned}
\begin{bmatrix} |x_1\rangle\langle x_2| - |y_1\rangle\langle y_2| \\ |x_1\rangle\langle y_2| + |y_1\rangle\langle x_2| \end{bmatrix} \xrightarrow{C_\phi} & \begin{bmatrix} cos(2\phi) & sin(2\phi) \\ -sin(2\phi) & cos(2\phi) \end{bmatrix} \begin{bmatrix} |x_1\rangle\langle x_2| - |y_1\rangle\langle y_2| \\ |x_1\rangle\langle y_2| + |y_1\rangle\langle x_2| \end{bmatrix} \\
= & \; Q_x[|x_1\rangle\langle x_2| - |y_1\rangle\langle y_2|] + Q_y[|x_1\rangle\langle y_2| + |y_1\rangle\langle x_2|]
\end{aligned}$$

$Q_x[|x_1\rangle\langle x_2| - |y_1\rangle\langle y_2|] + Q_y[|x_1\rangle\langle y_2| + |y_1\rangle\langle x_2|]$, is invariant with respect to C_ϕ. Where Q_x and Q_y represent the x and y components of the e_{2u} mode.

Now a C_2' rotation transforms $(|x_1\rangle, |y_1\rangle)$, $(|x_2\rangle, |y_2\rangle)$ and (Q_x, Q_y) to $(-|x_1\rangle, |y_1\rangle)$, $(|x_2\rangle, -|y_2\rangle)$ and $(-Q_x, Q_y)$, respectively. Therefore,

$$\begin{aligned}
Q_x[|x_1\rangle\langle x_2| - |y_1\rangle\langle y_2|] + Q_y[|x_1\rangle\langle y_2| + |y_1\rangle\langle x_2|] \xrightarrow{C_2'} & (-Q_x)[(-|x_1\rangle)\langle x_2| - |y_1\rangle(-\langle y_2|)] \\
& +Q_y[(-|x_1\rangle)(-\langle y_2|) + |y_1\rangle\langle x_2|] \\
= & \; Q_x[|x_1\rangle\langle x_2| - |y_1\rangle\langle y_2|] + Q_y[|x_1\rangle\langle y_2| + |y_1
\end{aligned}$$

is also invariant with respect to C_2' rotation.

Similarly a C_2'' rotation transforms $(|x_1\rangle, |y_1\rangle)$, $(|x_2\rangle, |y_2\rangle)$ and (Q_x, Q_y) to $(|x_1\rangle, -|y_1\rangle)$,

$(-|x_2\rangle, |y_2\rangle)$ and $(-Q_x, Q_y)$, respectively. and

$$\begin{aligned} Q_x[|x_1\rangle\langle x_2| - |y_1\rangle\langle y_2|] + Q_y[|x_1\rangle\langle y_2| + |y_1\rangle\langle x_2|] &\xrightarrow{C_2''} (-Q_x)[|x_1\rangle(-\langle x_2|) - (-|y_1\rangle)\langle y_2|] \\ &\quad +Q_y[|x_1\rangle\langle y_2| + (-|y_1\rangle)(-\langle x_2|)] \\ &= Q_x[|x_1\rangle\langle x_2| - |y_1\rangle\langle y_2|] + Q_y[|x_1\rangle\langle y_2| + |y_1\rangle\langle x_2|] \end{aligned}$$

is invariant with respect to C_2'' rotation also.

Considering the symmetry invariance with respect to the operations given above the $E_{1g} - E_{1u}$ PJT coupling matrix for the e_{2u} vibrational mode is given by

$$\mathcal{H}_{e_{2u}}^{PJT} = \begin{pmatrix} E_{E_{1g}}^x & 0 & \lambda Q_x & \lambda Q_y \\ 0 & E_{E_{1g}}^y & \lambda Q_y & -\lambda Q_x \\ \lambda Q_x & \lambda Q_y & E_{E_{1u}}^x & 0 \\ \lambda Q_y & -\lambda Q_x & 0 & E_{E_{1u}}^y \end{pmatrix}$$

The PJT coupling matrix for the a_{2u} mode can be derived similarly as follows.

$$\begin{aligned} |x_1\rangle\langle x_2| + |y_1\rangle\langle y_2| &\xrightarrow{C_\phi} [cos^2(\phi) + sin^2(\phi)][|x_1\rangle\langle x_2| + |y_1\rangle\langle y_2|] \\ &= [|x_1\rangle\langle x_2| + |y_1\rangle\langle y_2|] \end{aligned} \tag{A7}$$

$$\begin{aligned} |x_1\rangle\langle x_2| + |y_1\rangle\langle y_2| &\xrightarrow{E} |x_1\rangle\langle x_2| + |y_1\rangle\langle y_2| \\ |x_1\rangle\langle x_2| + |y_1\rangle\langle y_2| &\xrightarrow[\phi=6,3,2]{C_\phi} |x_1\rangle\langle x_2| + |y_1\rangle\langle y_2| \\ |x_1\rangle\langle x_2| + |y_1\rangle\langle y_2| &\xrightarrow{C_2'} -|x_1\rangle\langle x_2| + |y_1\rangle(-\langle y_2|) = -[|x_1\rangle\langle x_2| + |y_1\rangle\langle y_2|] \\ |x_1\rangle\langle x_2| + |y_1\rangle\langle y_2| &\xrightarrow{C_2''} -[|x_1\rangle\langle x_2| + |y_1\rangle\langle y_2|] \\ |x_1\rangle\langle x_2| + |y_1\rangle\langle y_2| &\xrightarrow{i} -[|x_1\rangle\langle x_2| + |y_1\rangle\langle y_2|] \end{aligned}$$

The characters of the a_{2u} mode are (1,1,1,1,-1,-1,-1) for (E, C_6, C_3, C_2, C_2', C_2'', i) operations in the D_{6h} symmetry point group. Thus $[|x_1\rangle\langle x_2| + |y_1\rangle\langle y_2|]Q_{a_{2u}}$ is invariant with respect to all symmetry operations of the D_{6h} point group. Similarly, it can be trivially shown that $[|x_1\rangle\langle y_2| - |y_1\rangle\langle x_2|]Q_{a_{1u}}$ is invariant with respect to all the symmetry operations of the D_{6h} point group. The PJT coupling Hamiltonian for the a_{2u} and a_{1u} vibrational modes is therefore given by

$$\mathcal{H}_{a_{2u},a_{1u}}^{PJT} = \begin{bmatrix} E_{E_{1g}}^x & 0 & \lambda' Q_{a_{2u}} & \lambda'' Q_{a_{1u}} \\ 0 & E_{E_{1g}}^y & -\lambda'' Q_{a_{1u}} & \lambda' Q_{a_{2u}} \\ \lambda' Q_{a_{2u}} & -\lambda'' Q_{a_{1u}} & E_{E_{1u}}^x & 0 \\ \lambda'' Q_{a_{1u}} & \lambda' Q_{a_{2u}} & 0 & E_{E_{1u}}^y \end{bmatrix} \tag{A8}$$

We mention that analysis of the *ab initio* electronic structure data reveal that the E_{1g}-E_{1u} PJT coupling is not relevant for HFBz.

References

[1] C. R. Brundle, M. B. Robin, and N. A. Kuebler, J. Am. Chem. Soc. **94**, 1466 (1972).

[2] H. Sponer, J. Chem. Phys. **22**, 234 (1954).

[3] C. D. Cooper, J. Chem. Phys. **22**, 503 (1954).

[4] K. N. Rao, H. Sponer, Can. J. Phys. **35**, 332 (1957).

[5] D. Phillips, J. Chem. Phys. **46**, 4679 (1967).

[6] R. Gilbert, P. Sauvageau, and C. Sandorfy, Can. J. Chem. **50**, 543 (1972).

[7] G. L. Loper, and E. K. C. Lee, Chem. Phys. Lett. **13**, 140 (1972).

[8] J. Metcalfe, M. G. Rockley, and D. Philips, J. Chem. Soc. Faraday Trans. 2. **70**, 1660 (1974).

[9] M. B. Robin, *Higher Excited States of Polyatomic Molecules*, Vol. III (Academic, New York, 1975), and references therein.

[10] C. B. Duke, K. L. Yip, G. P. Ceaser, A. W. Potts, and D. G. Streets, J. Chem. Phys. **66**, 256 (1976).

[11] R. P. Frueholz, W. M. Flicker, O. A. Mosher, and A. Kuppermann, J. Chem. Phys. **70**, 3057 (1979).

[12] R.P. Frueholz, W.M. Flicker, O.A. Mosher, A. Kuppermann, Chem. Phys.Lett. **52**, 86. (1977)

[13] J. Philis, A. Bolovinos, G. Andritsopoulos, E. Pantos, and P. Tsekeris, J. Phys. B: At. Mol. Phys. **14**, 3621 (1981).

[14] A. P. Hitchcock, P. Fischer, A. Gedanken, M. B. Robin, J. Phys. Chem. **91**, 531, (1987).

[15] D. R. Smith, J. W. Raymonda, Chem. Phys. Lett. **12**, 269, (1971).

[16] D. V. O'connor, M. Sumitani, J. M. Morris, and K. Yoshihara, Chem. Phys. Lett. **93**, 350 (1982).

[17] O. Plashkevych, L. Yang, O. Vahtras, and L. G. M. Pettersson, Chem. Phys. **222**, 125 (1997).

[18] C. D. Keefe, J. Barrett, and L. L. Jessome, J. Mol. Struc. **734**, 67 (2005).

[19] M. Z. Zgierski, T. Fujiwara, and E. C. Lim, J. Chem. Phys. **122**, 144312 (2005).

[20] C. Motch, A. Giuliani, J. Delwiche, P. Limao-Vieira, N. J. Mason, S. V. Hoffmann, and M. -J. Hubin-Franskin, Chem. Phys. **328**, 183, (2006).

[21] D. M. P. Holland, D. A. Shaw, M. Stener, and P. Decleva, J. Phys. B: At. Mol. Opt. Phys. **42**, 245201 (2009)

[22] H. Studzinski, S. Zhang, Y. Wang, and F. Temps, J. Chem. Phys. **128**, 164314 (2008).

[23] S. H. Lee, C. Y. Wu, S. K. Yang, and Y. P. Lee, J. Chem. Phys. **125**, 144301 (2006).

[24] I. Pugliesi, N. M. Tonge, and M. C. R. Cockett, J. Chem. Phys. **129**, 104303 (2008).

[25] T. Mondal, and S. Mahapatra, J. Chem. Phys. **133**, 084304 (2010).

[26] T. Mondal, and S. Mahapatra, J. Chem. Phys. **133**, 084305 (2010).

[27] E. Gindensperger, I. Bâldea, J. Franz, and H. Köppel, Chem. Phys. **338**, 207 (2007).

[28] S. Faraji, and H. Köppel, J. Chem. Phys. **129**, 74310 (2008).

[29] S. Faraji, H. -D. Meyer, and H. Köppel, J. Chem. Phys. **129**, 74311 (2008).

[30] T. Mondal, and S. Mahapatra, Phys. Chem. Chem. Phys. **11**, 10867 (2009).

[31] J. G. Philis, T. Mondal, and S. Mahapatra, Chem. Phys. Lett. **495**, 187 (2010).

[32] H. Sponer, D. Nordheim, A. L. Sklar and E. Teller, J. Chem. Phys. **7**, 207, (1939)

[33] H. A. Jahn and E. Teller, Proc. R. Soc. London, Ser. A **161**, 220. (1937)

[34] H. Köppel, W. Domcke, and L. S. Cederbaum, Adv. Chem. Phys. **57**, 59 (1984).

[35] M. Döscher, H. Köppel, and P. Szalay, J. Chem. Phys. **117**, 2645, (2002)

[36] T. S. Venkatesan, H.-D. Meyer, H. Köppel, L. S. Cederbaum and S. Mahapatra, J. Phys. Chem. A, **111**, 1746, (2007).

[37] W. Domcke, D. R. Yarkony and H. Köppel, *Conical Intersections: Electronic Structure, Dynamics and Spectroscopy*, World Scientific: Singapore, (2004).

[38] E. Teller, J. Phys. Chem. **41**, 109 (1937); G. Herzberg, and H. C. Longuet-Higgins, Discuss. Farad. Soc. **35**, 77 (1963); T. Carrington, Discuss. Farad. Soc. **53**, 27 (1972); D. R. Yarkony, Acc. Chem. Res. **31**, 511 (1998); F. Bernardi, M. Olivucci, and M. A. Robb, Chem. Soc. Rev. **25**, 321 (1996).

[39] M. Baer and G. D. Billing, *The Role of Degenerate States in Chemistry*:Advances in Chemical Physics, Vol. 124, Wiley: Hoboken, (2002).

[40] H. Köppel, L.S. Cederbaum, and S. Mahapatra, *Theory of the JahnTeller Effect. Handbook of High-resolution Spectroscopy*, John Wiley & Sons, (2011).

[41] S. Mahapatra, Acc. Chem. Res. **42**, 1004 (2009).

[42] S. Mahapatra, Int. Rev. Phys. Chem. **23**, 483 (2004).

[43] M. Born, and R. Oppenheimer, Ann. Physik (Leipzig) **84**, 457 (1927).

[44] W. Lichten, Phys. Rev. **164**, 131 (1967); F. T. Smith, ibid. **179**, 111 (1969); T. F. O'Malley, Adv. At. Mol. Phys. **7**, 223 (1971); T. Pacher, L. S. Cederbaum, and H. Köppel, Adv. Chem. Phys. **84**, 293 (1993).

[45] H. Sekino, and R. J. Bartlett, Int. J. Quantum. Chem., Chem. Symp. **18**, 255 (1984); J. Geertsen, M. Rittby, and R. J. Bartlett, Chem. Phys. Lett. **164**, 57 (1989); J. F. Stanton, and R. J. Bartlett, J. Chem. Phys. **98**, 7029 (1993).

[46] R. D. Amos, A. Bernhardsson, A. Berning, P. Celani, D. L. Cooper, M. J. O. Deegan, A. J. Dobbyn, F. Eckert, C. Hampel, G. Hetzer, et al., MOLPRO, a package of ab initio programs designed by H. -J. Werner, P. J. Knowles, version 2008.1.

[47] G. A. Worth, M. H. Beck, A. Jäckle and H. -D. Meyer, The MCTDH Package, Version 8.2, 2000, University of Heidelberg, Germany. H. -D. Meyer, Version 8.3, 2002. Version 8.4 (2007), See http://www.pci.uni-heidelberg.de/tc/usr/mctdh/

[48] H. -D. Meyer, U. Manthe, and L. S. Cederbaum, Chem. Phys. Lett. **165**, 73 (1990).

[49] U. Manthe, H. -D. Meyer, and L. S. Cederbaum, J. Chem. Phys. **97**, 3199 (1992).

[50] H.-D. Meyer and G. A. Worth, Theor. Chem. Acc. 109, 251 (2003).

[51] T. H. Dunning, Jr., J. Chem. Phys. **90**, 1007 (1989).

[52] M. J. Frisch et al., Gaussian 03, revision B.05; Gaussian, Inc., Pittsburgh, PA, 2003.

[53] A. Almenningen, O. Bastiansen, R. Seip, M. Hans, Acta Chem. Scand. **18**, 2115 (1964).

[54] E. B. Wilson Jr., J. C. Decius and P. C. Cross, *Molecular vibrations* (McGraw-Hill, New York, 1955).

[55] G. Herzberg, *Infrared and Raman Spectra of Polyatomic Molecules, Vol.2 of Molecular Spectra and Molecular Structure* (Van Nostrand, New York, 1945) p. 183.

[56] E. B. Wilson, Jr., Phys. Rev. **45**, 706 (1934).

[57] D. Steele and D. H. Whiffen, Trans. Faraday Soc., **55**, 369 (1959)

[58] A. Bergner, M. Dolg, W. Kuechle, H. Stoll, and H. Preuss, Mol. Phys. **80**, 1431 (1993).

[59] W. Domcke, H. Köppel, and L. S. Cederbaum, Mol. Phys. **43**, 851 (1981).

[60] J. Cullum, and R. Willoughby, *Lanczos Algorithms for Large Symmetric Eigenvalue Problems* (Birkhäuser, Boston, 1985) Vols. I and II.

[61] I. B. Bersuker, *The Jahn-Teller effect*, (Cambridge University Press, Cambridge (U.K), 2006); I. B. Bersuker, Chem. Rev. **101**, 1067, (2001).

[62] J. C. Slonczewski, Phys. Rev. **131**, 1596 (1963); J. C. Slonczewski, and V. L. Moruzzi, Physics **3**, 237 (1967)

[63] P. Habitz, W. H. E. Schwarz, Theo. Chem. Acta. **28**, 267 (1973); H. Köppel, E. Haller, L. S. Cederbaum, and W. Domcke, Mol. Phys. **41**, 669 (1980)

[64] B. Milian-Medina, S. Varghese, R. Ragni, H. Boerner, E. Orti, G. M. Farinola, and J. Gierschner, J. Chem. Phys. **135**, 124509 (2011)